DEVELOPMENT OF QUANTITATIVE TECHNIQUES FOR LITHIUM COMPOUNDS FOR NEXT GENERATION BATTERIES WITH FOCUSED ION BEAM SCANNING ELECTRON MICROSCOPY

Stéphanie Bessette

Department of Mining and Materials Engineering
McGill University
Montréal, Québec, Canada
September, 2018

A thesis submitted to McGill University in partial fulfillment of the requirements of the degree of Masters of Engineering in the Department of Mining and Materials Engineering

© Stéphanie Bessette, 2018.

TABLE OF CONTENTS

LIST OF FIGURES

LIST OF TABLES

LIST OF ACRONYMS

LiB	Lithium-ion battery
SEI	Solid electrolyte interface
SEM	Scanning electron microscopy
FIB	Focused ion beam
FIB-SEM	Dual beam microscope
HV	High vacuum
UHV	Ultra high vacuum
SIMS	Secondary ion mass spectrometry
TOF-SIMS	Time-of-flight secondary ion mass spectrometry
SE	Secondary electron
BSE	Backscattered electron
SI	Secondary ion
PI	Primary ion
WD	Working distance
MFP	Mean free path
EDS	Energy dispersive X-ray spectroscopy
E_c	Critical ionization energy
UTW	Ultra-thin window
MAC	Mass absorption coefficient
Z	Atomic number
FWHM	Full width at half maximum
ZAF	Atomic number/absorption/fluorescence correction
EELS	Electron energy-loss spectroscopy
ZLP	Zero-loss peak
NMC	Nickel manganese cobalt oxide
LFP	Lithium iron phosphate or $LiFePO_4$
m/z	Mass-to-charge ratio
RSF	Relative sensitivity factor

ABSTRACT

Electric vehicles have started to make their appearance in the transportation industry. At Quebec's scale especially, since electricity is already sustained by an extensive network of dams and reservoir, Hydro-Quebec puts a lot of focus towards green gas emission reduction via transportation electrification. To be widely accepted, batteries used in electric vehicles must have high ranges, long durability, be safe and an economical choice in the long run for its user to abandon gasoline-powered automobiles. In that matter, the company's Center of Excellence in Transportation Electrification and Energy Storage works tirelessly on the development of new generation battery materials using elements available in large quantities, with high performance chemistry. Materials characterization with Scanning Electron Microscopy is one of the most important steps in developing new materials, since it links the microstructure of the material to its fabrication process and properties down to the nanometer scale.

This study focuses on the development of quantitative techniques for lithium in battery materials since this light element is the key element in the operation of a battery. In this work energy dispersive X-ray spectroscopy (EDS), electron energy-loss spectroscopy (EELS) and secondary ion mass spectrometry are evaluated in relation to their capabilities to both detect and quantify lithium atoms in battery materials. A portable time-of-flight secondary ion mass spectrometer (TOF-SIMS) that can attach to a standard dual beam microscope (FIB-SEM) was found to fulfill both aspects while allowing high resolution imaging and chemical analysis of the samples. An experimental calibration curve of lithium content in standard nickel cobalt manganese oxide cathodes was built using TOF-SIMS detector. The calibration curve allows identification of lithium content in cathodes with different state of charge and according to different charging rates. TOF-SIMS allows visualization of ionic distributions in material. Furthermore, it can help observe differences in crystallographic orientation with respect to the beam in between primary particles and permits identification of chemical hotspots of lithium.

RÉSUMÉ

De plus en plus, les voitures électriques font leur apparition sur le marché de l'automobile. À l'échelle du Québec plus particulièrement, comme la majorité de l'électricité utilisée de façon domestique et industrielle provient d'un vaste réseaux hydroélectrique, le focus d'Hydro-Québec envers la réduction des émissions de gaz à effet de serres se tourne vers l'électrification des transports. Pour que le grand public délaisse la voiture à essence au profit de la voiture électrique, les batteries proposées dans ces véhicules doivent permettre une grande autonomie, être durables en plus d'être sécuritaires et se révéler un choix économique à long terme pour l'acheteur. Selon cette perspective, le Centre d'Excellence en Électrification des transports et Stockage d'Énergie d'Hydro-Québec s'acharne à développer des matériaux de batteries utilisant des éléments disponibles en grandes quantités et économiques en plus de d'une chimie de haute performance. La caractérisation des matériaux à l'aide d'un microscope électronique à balayage est l'une des étapes les plus importantes dans la recherche et développement, puisqu'elle peut nous indiquer à chaque étape de la vie utile d'une batterie les liens entre la microstructure, les processus de fabrication et ses propriétés et ce, jusqu'au nanomètre.

Ce travail porte sur le développement de techniques quantitatives pour le lithium dans les matériaux de batteries puisque celui-ci est l'élément clé de leur fonctionnement. Dans cette étude, les techniques de spectroscopie des rayons X par dispersion d'énergie (EDS), de spectroscopie des pertes d'énergie des électrons (EELS) et la spectrométrie de masse à ionisation secondaire (SIMS) seront évaluées par rapport à leur capacité à détecter et à quantifier le lithium dans les matériaux de batteries. Un détecteur portable d'ion secondaires par temps de vol (TOF-SIMS) s'est révélé le meilleur choix parmi ces techniques en permettant l'imagerie haute résolution du lithium et son analyse chimique et quantitative. Une courbe de calibration expérimentale du contenu en lithium dans des cathodes standard d'oxide de nickel cobalt manganese a pu être construite grâce au TOF-SIMS. Cette courbe de calibration permet l'identification de la concentration de lithium dans l'échantillon en fonction de l'état de charge de la cathode et selon différent taux de charge. Le TOF-SIMS permet de surcroît la visualisation des distributions des ions dans le matériaux. Il a permis de voir des différences dans l'orientation cristalline des grains primaires et l'identification de points chaud ou "hotspots" de lithium.

CONTRIBUTION OF AUTHORS

This thesis prepared as a requirement of the degree of Masters of Engineering (M. Eng) in the Department of Mining and Materials Engineering consists of one manuscript entitled *Nanoscale Lithium Quantification in* $Li_xNi_yCo_wMn_zO_2$ *as Cathode for Rechargeable Batteries*. The candidate is the primary author of the manuscript. The manuscript is co-authored by researchers from Hydro-Québec's battery research center, the Center of Excellence in Transportation Electrification and Energy Storage who provided samples for analysis and help for electrochemical data interpretation. In addition, Dr. Karim Zaghib, director of the center of Excellence, provided the instruments and facilities. Both Dr. Zaghib and Professor Raynald Gauvin are listed as co-authors in their capacity as research supervisors. The candidate conducted all experiments, sample preparation and analysis regarding this manuscript. All other chapters of this thesis were written entirely by the candidate.

ACKNOWLEDGEMENTS

The author would like to acknowledge the help of Hydro-Québec personnel and McGill fellow students and faculty members over the course of the last two years: Thanks to Prof. Raynald Gauvin, for his academic support and guidance. Thanks to Dr. Karim Zaghib for providing the opportunity to join his research team at the Center of Excellence in Transportation Electrification and Energy Storage and to work on this exciting project. Special thanks to Pierre Hovington for his supervision and guidance, and for introducing me to microscopy and material science in the first place. Thanks to Daniel Clément and Vincent Gariépy for their technical help and training through my thesis as well as their overall support. Thanks to Chisu Kim, Catherine Gagnon and Patrick Bouchard for providing the samples used in this project. Thanks to Andrea Paolella and Hendrix Demers for their interesting discussions and Michel Roy for his technical support and knowledge about the microscopes. Thanks to my fellow student colleagues Maryam Golozar, Rachel Lévesque-Bélanger, François Larouche and past collaborators such as Hugues Marceau and all my friends from undergraduate studies for their help and support. Finally, thanks to my parents, Josée Surprenant and Robert Bessette, as well as my sister Caroline for their unconditional love and support throughout all of my studies and to my boyfriend Guillaume Emond for his neverending patience and support during the last two years.

CHAPTER 1 INTRODUCTION

1.1 Motivation

The rise of international concerns about climate change and the role of human action in it has lead many countries to take significant actions in order to reduce their greenhouse gas emission and carbon footprint, particularly recently with the ratification of the Paris agreement in 2016, which counts 175 countries to this date [1]. As a result, alternative means of generating electricity relying on renewable resources such as solar, wind power, biomass as well as hydroelectricity, have in the last decades seen an increase in popularity and will see an increase in funding over the next few years to meet 2030's reduction targets. In addition, a shift towards transportation electrification is seen in countries like Canada [2] and electric vehicles are also starting to be more accessible to the average citizen all around the world. In order for this shift to fully sustainable and green energy sources to continue and prosper, storage issues have to be assessed and therefore more research has to be done on battery materials.

Hydro-Québec has been a prolific actor on the Québec scene. More than 99% of the electricity produced by this government owned company comes from renewable resources, mainly hydroelectricity [3]. Hydro-Québec also has a research center that focuses on development of new battery materials for electric vehicle applications, which has generated over 800 patents and 60 licences related to next generation battery materials [4, 5]. The company intends on participating further in Québec's transportation electrification by targeting several specific criteria for tomorrow's batteries: improving battery safety, performance, reducing manufacturing costs all while integrating eco-friendly and recyclable materials [3].

Hydro-Québec has been studying lithium for battery material applications for over 25 years. Scanning electon microscopy (SEM) analysis is a big part of electrode material development as it can reveal the links between the microstructure, the making processes and failure modes of a battery. The multiple signals generated by the interaction of the electron beam with the

specimen allows determination of a sample's morphology, structure and chemical composition with Energy dispersive X-ray spectroscopy (EDS) from millimeter to nanometer scale. This ability to conduct chemical and structural analyses within the same instrument makes SEMs incredibly powerful and polyvalent tools. Lithium is the key element in battery operation since its ionic conductivity allow the electrochemical reactions to happen. Therefore determining its concentration in a sample is important. However, even windowless EDS detectors are limited towards Li K x-ray detection because of its low energy ($\sim$ 55 eV) and its quantification is made even more difficult by very low signal resulting from lithium's x-rays high Mass absorption coefficient (MAC) in the material, low fluorescence yield (ω_i=10^{-4}) and complex emission process.

1.2 Objectives

The objective of this thesis is to develop new techniques for lithium quantification in battery materials using SEM. Quantifying lithium in electrodes will reveal information not only about the structure of the materials but also completeness of electrochemical reactions and provide insight on failing processes. Chapter 2 will present the characterization techniques that are typically used to analyze lithium in materials, namely EDS, Electron energy-loss spectroscopy (EELS) and Secondary ion mass spectrometry (SIMS). The latter allows identification and quantification of the components of a sample by the bombardment of its surface by energetic primary ions. It has full periodic table coverage and the association of a SIMS with a Focused ion beam (FIB) microscope allows the analysis of very small analytical volumes - as small as the FIB's spatial resolution [6]. Dual-beam microscopes (FIB-SEM) are therefore suitable instruments for battery material applications, providing visualization and elemental quantification. Chapter 3 will assess the methodology used for sample preparation and analysis. Chapter 4 will present the characterization work done on standard Nickel manganese cobalt oxide (NMC) cathodes with Time-of-flight secondary ion mass spectrometry (TOF-SIMS).

CHAPTER 2 LITERATURE REVIEW

Before entering the quantitative characterization of lithium compounds, a review of the lithium-ion battery technology will be made. Then, it is important to fully understand the techniques that are nowadays used to detect and quantify lithium but also their limitations regarding this material. In this chapter, the principle of the FIB-SEM and its components will be first explained. Then the basic operation of EDS, EELS, SIMS, and more particularly TOF-SIMS, as well as their quantitative principles will be discussed. Finally, common applications of SIMS and TOF-SIMS on battery materials will be reviewed since this technique will be the focus of this work.

2.1 The lithium-ion battery

A battery is an electrochemical device composed of a positive electrode (cathode), a negative electrode (anode) and an electrolyte. By definition, an electrochemical device is one where the combined action of electrical and chemical phenomenon are in effect [7]. The electrodes are by definition electronic conductors and the electrolyte acts as the ionic conductor, allowing the oxidation (electron loss) and reduction (electron gain) reactions to happen in the device. In a rechargeable lithium battery, electrons travel in the external circuit from the cathode to the anode during charging, while the lithium ions diffuse in the electrolyte from the cathode and are reduced at the anode. The opposite processes take place during discharge.

The capacity (C) of a battery defines the charge or energy stored in the battery. It is commonly expressed in terms of ampere-hours (Ah). To compare the different materials used in a battery, knowledge of the specific capacity is needed. It is a measure of the total capacity per gram of active material (Ah g^{-1}). Batteries can be charged and discharged at different speeds, called C-rates, which will define the current to apply according to the battery's capacity. A current of 1C means the battery will be completely discharged in 1 hour, C/2 in two hours with a current that is half as large and so on. The State-of-Charge (SOC) of a battery is a notion used to characterize state of the battery in function of the percentage of capacity present. Therefore, a SOC of 50% means that 50% of the capacity of the device is still present. At the end of charging, the device is at a SOC of 100%, the anode is fully lithiated (x of Li = 1), while the cathode is fully delithiated (x=0).

The principle of Lithium-ion batteries (LiB) relies on the following oxidation reaction

$$Li \rightarrow Li^{+} + e^{-} \tag{2.1}$$

The electron produced is introduced in the cathode by the external circuit. Typically, metallic oxides are used as cathode materials [8], mainly because they act as intercalation compounds, allowing the lithium ions to be inserted into the porous structure of the material while remaining structurally stable during the electrochemical process [9]. The typical anode used

in LiB is graphite (Li_xC_6) both for its high cycle life and its specific capacity [10] which is another intercalation compound, although $Li_4Ti_5Co_12$ (LTO) is greatly commercialized. However, lithium metal foil would be the ideal anode material, mainly because its lightness (6.941 g mol-1) and density (0.51 g cm-3) would allow higher energy densities and lighter batteries, and because of its high electroactivity [9]. Lithium has a specific capacity of 3861 mAh g^{-1} which explains its appeal compared to graphite's 372 mAh g^{-1} [11].

Although lithium metal is a promising material for high energy batteries, dendrite formation is a barrier that led to the larger commercialization of carbon based anodes, graphite in particular [12]. These needle like structures can form bridges between both electrodes and result in short-circuiting or even explosion of the device. Many studies have been dedicated to their characterization and growth mechanisms with a focus on how to inhibit their growth in pure metals or alloys [13–20]. Focus towards solid state batteries using polymer electrolytes or even ceramics is underway. Use of solid electrolyte can provide additional mechanical support to the device and can hamper dendrite propagation. Solid electrolyte interphase (SEI) is formed during the first charge as a result of electrolyte decomposition can enhance the stability of the battery, preventing further decomposition [21]. However, during its formation, the SEI consumes irreversibly a certain quantity of lithium ions resulting incapacity loss [22]. Furthermore, in order to improve the battery's stability, the SEI layer must be uniform [23]. Heterogeneity in the thickness and the composition of SEI layer can be the seed of dendrite growth, which can lead to battery failure, as will be explained earlier [24]. The SEI thickening with increasing cycles is another important problematic of LiB.SEI is very poorly conductive and therefore hinder the good operation of the battery [9]. Other aging mechanisms can also alter the good functioning of a battery. Some examples consist in the electrolyte decomposition that can lead to production of undesirable by products (ex. HF), volume expansion that may results in cracking and reduction of porosity in the material, limiting lithium insertion by decreasing the total contact area between active material and electrolyte [25].

2.2 The FIB-SEM microscope

A dual-beam microscope contains in a single system an electron column (SEM) and an ion column (FIB) positioned typically around 55° from the vertical. An intersection point at a defined working distance allows both visualization of the sample in SEM and FIB imaging and permits monitoring while cross-section milling, which provides an interesting advantage compared to FIB single systems [26]. Moreover, this configuration allows chemical analysis (by enabling the use of an EDS detector), electron and ionic imaging, as well a three-dimensional structural analysis of materials. For this research project the FIB-SEM microscope used is a TESCAN LYRA3 equipped with a tungsten field emission SEM (FE-SEM) and a gallium ionic column.

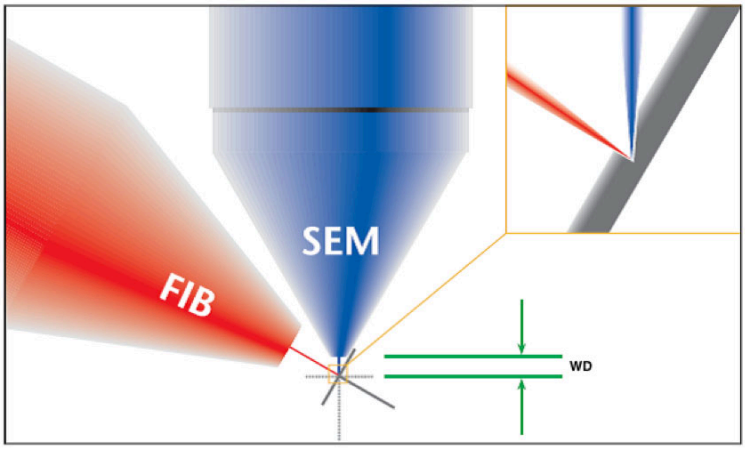

Figure 2.1 Configuration of a typical dual-beam system in [26] from FEI

2.2.1 Scanning electron microscopy

The electron gun generates the electrons by thermionic emission from a tungsten (W) filament and accelerates them to the desired potential, in a range of 0.1 keV to 30 keV. Lenses are then used to demagnify the emerging beam and properly focus it onto the specimen. A series of magnetic lenses accomplish this task, starting with a condenser lens, and finishing by the objective lens. Apertures are also used in the column to limit the quantity of electrons passing in each lens and to restrain the convergence angle of the beam to low values, which helps reducing the aberrations in the objective lens. The scanning action strictly speaking

is produced by the deflection system located before the final objective lens. Two pairs of deflection coils - one for each direction - deviate the electron beam on an x-y pattern on the specimen. Deviation of the beam is made by adjusting the electromagnetic strength of the coils and will permit the formation of SEM images of the irradiated region. Electrons exiting the objective lens will travel a certain distance in the vacuum of the microscope chamber, called working distance (WD), before striking the specimen which is mounted on a motorized stage. In the TESCAN FIB-SEM, observation of the specimen with the SEM is made at normal incidence (90°). Electron beam-specimen interactions will lead to secondary electron and backscattered electron emissions that can be collected using various detectors placed at different positions in the microscope chamber. The whole imaging system if made possible by the action of vacuum pumps, who maintain the microscope chamber to pressures of $10^{-}4$ Pa to avoid contamination of the W filament by oxidation and contamination of the specimen [27].

The secondary electrons (SE) produced in the interaction volume can be collected with a traditional Everhart-Thornley (ET) detector. Resulting from inelastic collisions in the sample, SE produced by the beam electrons are by definition electrons emitted with energies lower than 50 eV [27]. Their very low energy and high energy loss rate implies that SE collected in the ET detector come from a region within 5λ of the specimen's surface, where λ is the typical distance between two collision events. SE images are therefore rich in surface details.

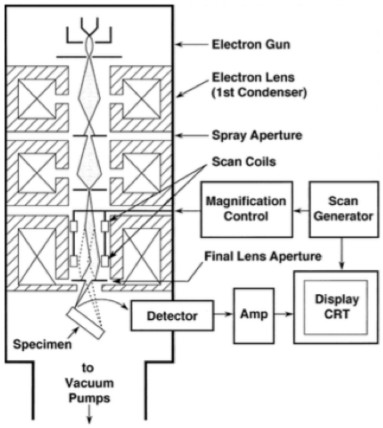

Figure 2.2 Schematic of the electron column [27]

Electrons which are subject to multiple high angle elastic collisions before exiting the specimen's surface with high remaining energy are called backscattered electrons (BSE). Knowing

that the amount of backscattered electrons is proportional the atomic number Z, SEM images can show high compositional contrast which can lead to identification of different phases in the material. However, no quantification can be done with BSE SEM images, which is why an EDS detector is traditionally mounted on SEM microscopes to permit quantification of the different phases obtained with the BSE signal. Description of EDS will be made in section 2.3.

A number of vacuum pumps are typically used to maintain a reduced pressure in the microscope chamber. Different types or combinations of pumps are used depending on the vacuum level required, which is directly linked to the contamination level that the specimen can undergo without the analyzes being impeded by the chemical changes induced by adsorption of gas particles at the specimen's surface. The typical entry-based SEM will normally work under High Vacuum (HV) conditions, from 10^{-3}–10^{-6} Pa (10^{-5}–10^{-8} Torr). Under these conditions, the mean free path (MFP) of gas molecules in the chamber is of the order of kilometers [27], which means the electron beam will reach the specimen sample (typically at WD $<$ 15 mm) without significant spreading due to collisions with the chamber's molecules. Only in variable pressure mode, mainly used for imaging of insulating or poorly conductive specimen, is the pressure as high as 100Pa and the MFP of the order of the working distance. Ultra High Vacuum (UHV) is required when surface conditions matter the most. Under UHV, the pressure in the microscope chamber is maintained $<10^{-7}$Pa ($<10^{-9}$ Torr), which means the MFP is 50 km and a monolayer of gas particles is absorbed at the specimen surface in about 4 days, compared to every other second under HV [27, 28] .

2.2.2 Focused ion beam

The FIB column is very similar to a typical electronic column, except that energetic gallium ions (Ga^+) instead of electrons are used in order to compute images of the material. The ion source is typically a W needle attached to a reservoir containing liquid Ga metal. The choice of Ga for commercial FIB is explained among others by its low melting point, low volatility and small energy spread during emission [26]. Once the W needled is wet by liquid Ga, extractor electrodes ionizes the Ga tip, causing its evaporation and allowing a current density of $\sim 10^8\ A/cm^2$ to pass through the next part of the ion column [26].

Ga ions are then accelerated to a known voltage, in the range of 0.5 to 30 keV and provide a resolution at the specimen of <5nm at 30 keV [30]. Similarly to SEM, the ions then pass through a series of lenses and apertures that shape the ionic beam into a focused probe at the specimen's surface. A set of scanning coils also renders an x-y pattern on the sample to form the FIB image. Since the ion beam is a destructive beam, beam blankers are used to limit specimen destruction while imaging is not performed.

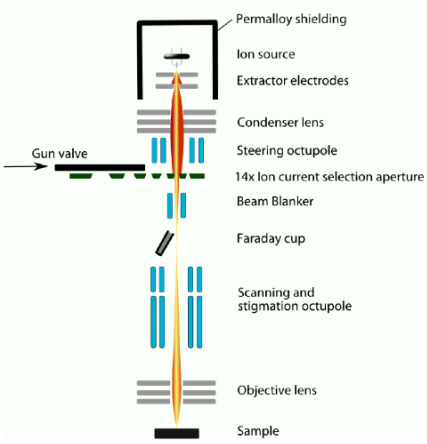

Figure 2.3 Ionic column [29]

Upon striking the specimen, the projectile's energy is transferred to the surface, causing collisions with the specimen's atoms and in between the sample's atoms. Ga ions are implanted in the material, transferring all their energy by elastic and inelastic collisions. When the energy transferred overcomes the displacement energy of an atom, it will be removed from its lattice site, and might be given enough kinetic energy to continue its course in the matrix and possibly create other vacancies [31]. If the displaced atom happens to be close to the surface, this results in sputtering. This process is commonly called a collision cascade from the beam impact which causes emission of secondary electrons, neutrals, secondary ions or molecules at low energy. It is possible to image the specimen by collecting FIB-induced secondary electrons with a multichannel plate positioned on the objective lens or an electron multiplier located at the side of the ion column. Since the Ga ions depth of penetration in the specimen is only of a few nanometers [26], SE produced will render strong topographical contrast of the specimen's surface. Also, channeling contrast can be observed from SE emission, so crystallographic information can be deduced from the sample. Secondary ions can be detected by the multiplier detector to which a bias is applied. SI imaging is less prone to charging, therefore it can be a useful tool for imaging non-conductive samples.

Ion dose

The ion dose is an important aspect of the FIB microscope. By definition, it is the number of ions impinging on a selected target area and that get absorbed in the material [26]. Its units are $ions/cm^2$. The ion dose is both proportional to the beam current and magnification of the image. It is directly linked to the damage or etching power of the ion beam in the material.

Amorphous & other intermetallic phases

The build-up of a surface amorphous phase on the specimen is one consequence of the primary ions (Ga^+) getting absorbed in the specimen. This irradiation damage causes changes in the crystallinity of the substrate, by destruction of the initial lattice structure of the material and can impede the qualitative and quantitative analysis. The width of the amorphous layer that is formed with the FIB is proportional to the penetration depth of the Ga ions in the material and 30 keV energy ion exposure has been proven to cause extensive damage to the material [33].

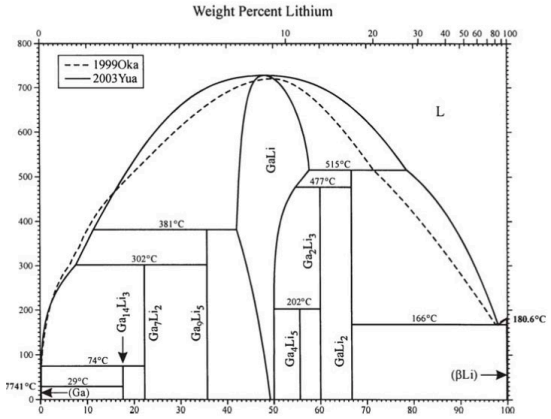

Figure 2.4 Ga-Li phase diagram [32]

For comparison purposes, the ion range of Ga ions accelerated at 30 keV into lithium is 100 nm, where as in typical battery compounds, like NMC and LFP, the ion range of 25 and 30 nm respectively, as simulated with Transport of Ion in Matter (TRIM) program (part of the Stopping and Range of Ion in Matter (SRIM) software [34].

Gallium is also known to form intermetallic phases with a number of elements, due to its low melting point [33]. In battery materials, lithium tends to form amalgams with Ga ion, which limits the accuracy of quantitative analysis. Figure 2.4 shows the phase diagram of Li-Ga

system. Eutectics $Li_q \leftrightarrow Ga_{14}Li_3 + Ga$ and $Li_q \leftrightarrow GaLi_2 + Li$ have been reported respectively at 29°C by Okamoto [32] and 28°C by Azza et al. [35] and was found by Okamoto at 166°C and Azza et al. at 164°C. The eutectic formation not only modifies the microstructure of the sample but also prevents further uniform milling of the samples. In copper, for example, Cu_3Ga phase formation during fibbing is known to be particularly difficult to mill [36].

The crystalline sample can also be subject to melting, formation of pools of liquid metal or even droplets of Ga [37]. Working under cryogenic temperatures has been proven to reduce damage and eutectic formation in Sn and semiconductor (group III-V elements) by bringing the crystallite to a temperature much lower than the eutectic, thus avoiding the eutectic reaction [37, 38]. Working at cryo temperature conditions has also proven to reduce damage and deformation from FIB-milling in soft materials as polymers and biological samples that are soft at room temperature [39].

Channeling effects

Crystallographic contrast can be seen in FIB secondary ion images due to channeling which by definition implies that ions may penetrate to greater distances in the material along a low index (example [110]) direction compared to non-channeling (high index) or amorphous phases because of the much lower stopping power in the low-index direction. The collision cross-section is indeed reduced along low-index planes, which leads to displacement of the collision cascade deeper in the material, since some ions may travel greater distances with little to no energy losses. This channeling effect therefore brings reduction of BSE and SE emission coefficient as well as a decreased sputter yield and an increased ion range. This results in SI and SE images in areas of dark intensity.

This channeling effect can be explained by visualizing the atomic rows and planes in the material as guides that propel the primary ions further in the material [40], as shown in figure 2.5. At one point, the ion will hit a defect in the crystal, enter another grain of a different crystalline orientation, suffer from an energy-loss inelastic collision or undergo a high angle Rutherford collision and exit the channel, a process called "dechanneling" [41].

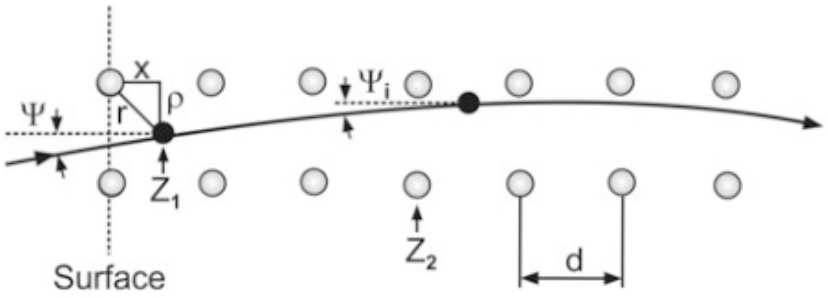

Figure 2.5 Schematic of atomic rows and planes acting as guides for the primary ions [42]

Channeling effects have also been linked with FIB milling conditions. Along or close to a crystalline direction, since the ions penetrate deeper because they undergo little nuclear collisions, the reduced sputtering yield lead to improved milling characteristics. The trenches made by the FIB have clean cut walls and a flat bottom, since the lower sputtering yield decreases the probability of redeposition [43]. On the contrary, along an amorphous or non-channeling direction, the ions face what seems to be a denser material, and hence are subject to high angle elastic scattering, which leads to an enhanced sputtering yield and a faster milling rate. This faster milling rate, result of a higher collision cross-section, leads to sloped trench walls because the redeposition of material is high [26]. Figure 2.6a shows this correlation between milling characteristics and channeling contrast.Finally, at the microscopic scale, when adjacent grains are of different crystallographic orientation, they won't experience the same effective milling rates from the ion beam, leading to increased topography of the sample, as demonstrated in figure 2.6b.

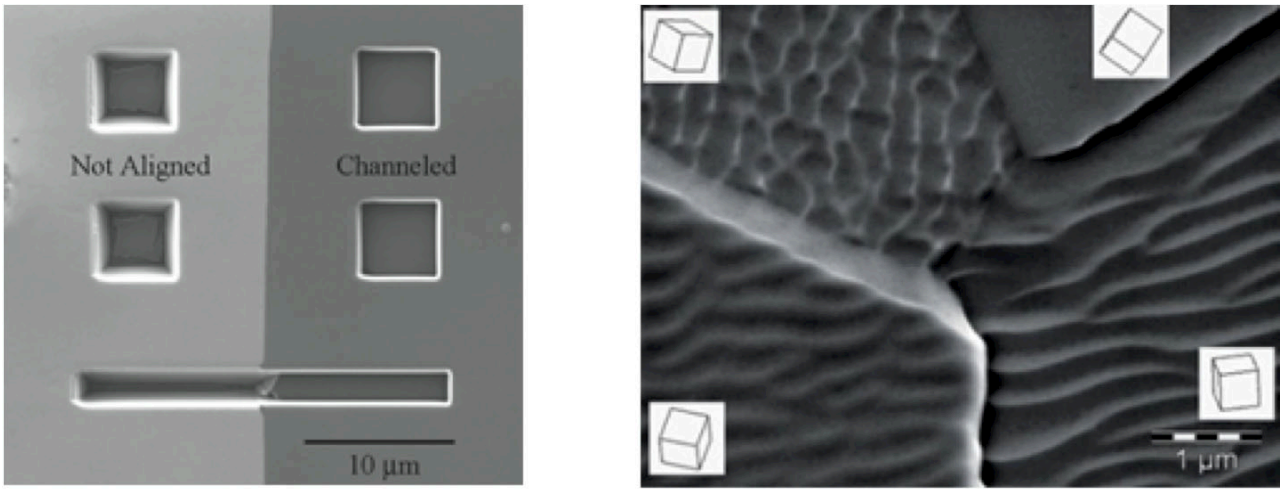

Figure 2.6 Channeling effects in FIB imaging. (a) Relationship between milling conditions, redeposition artifacts and crystallographic orientation shown in a Cu crystal [26] and (b) Effect of different crystallographic orientation in adjacent grains [44]

2.3 EDS & its quantitative analysis

Primary beam electrons also generate x-rays in the sample by creating vacancies in the inner shells of the sample's atoms. For a shell electron to be removed, the energy of the incoming beam electron must be equal or greater to the critical ionization energy (E_c) of that specific electron. Then, relaxation of an upper shell electron to fill the vacancy in the inner shell results in x-ray generation or emission of an Auger electron with energy characteristic to the difference between the two shells involved. An x-ray is produced when relaxation results in photon emission while Auger emission happens when the energy difference is transferred to an outer shell atom, ejecting it from the sample's atom. Light elements will only produce K series x-rays (L→ K transition), while atoms of higher Z number can produce L (M → L) and even M x-rays (N → M) for heavy elements [27]. Because of the energy range of SEM operation, which is up to 30 keV, some element's x-ray lines will not be ionized, especially for high Z atoms. The produced x-rays are collected by an EDS detector placed in the microscope chamber. An x-ray spectrum results from the measurement which can help one to conduct localized qualitative and quantitative chemical analysis of the desired sample. The fluorescence yield ω represents the probability of x-ray generation over the total number of ionizations. The fluorescence yield is a strong function of atomic number Z, as shown by equation 2.2 where Z is the atomic number and a is a constant related to the shell in question.

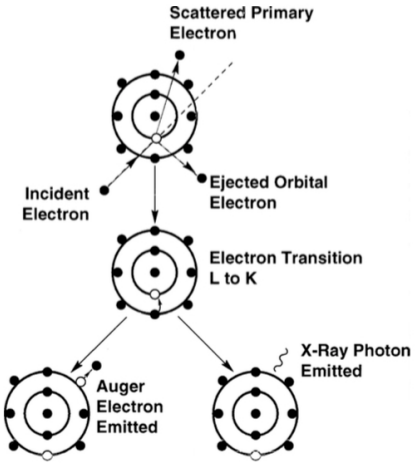

Figure 2.7 X-ray and Auger emission process following excitation of an atom by electron [27]

$$\omega_i = \frac{Z^4}{a + Z^4} \text{ [45]} \tag{2.2}$$

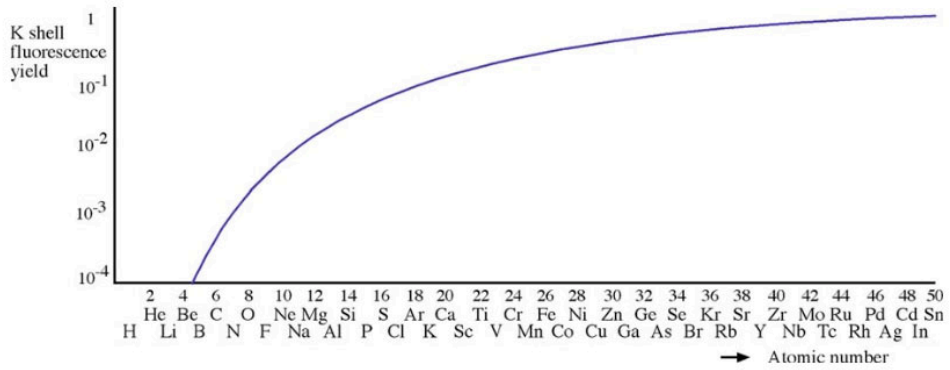

Figure 2.8 Variation of the fluorescence yield ω with the atomic number Z for the K inner shell [45]

From figure 2.8 and equation (2.2), we can see that x-ray generation is a favored process for heavy elements, while for light elements Auger emission dominates the outcome of ionization events [27], since the Auger yield is complementary to the fluorescence yield.

2.3.1 Components

X-rays generated in the sample and who successfully travel through layers of the specimen are emitted almost isotropically, but a certain angular distribution comes from the fact that some x-rays are generated at various depths [46]. As x-ray intensities increase with increasing take-off angles, the working distance of the FIB-SEM apparatus calls for an optimal position of the EDS detector, which is usually placed laterally, at angles close to 45° of the sample's normal. X-rays emitted in the direct solid angle of the detector will first pass through a thin window that serves the function of isolating the detector from the specimen chamber [27], before being absorbed by the detector, a lithium doped silicon crystal also referred to as Silicon Drift Detector (SDD). The absorbed x-ray will lead to the creation of a photoelectron. By travelling in the crystal, this photoelectron will give up all is energy in the form of electron-hole pairs. The electrons created by one single photoelectron will represent a charge proportional to the incident x-ray that will be converted to a voltage by a field-effect transistor (FET) preamplifier. In order to minimize noise, the crystal and preamplifier are placed in a cryostat that keeps the temperature in the device at around liquid nitrogen's.

The voltage signals are then amplified and passed through a multi-channel analyzer (MCA) that sorts the incoming voltage pulses into different channels corresponding to specific energy ranges. Finally, the pulses are being displayed as histograms of intensity vs x-ray energy on the computer.

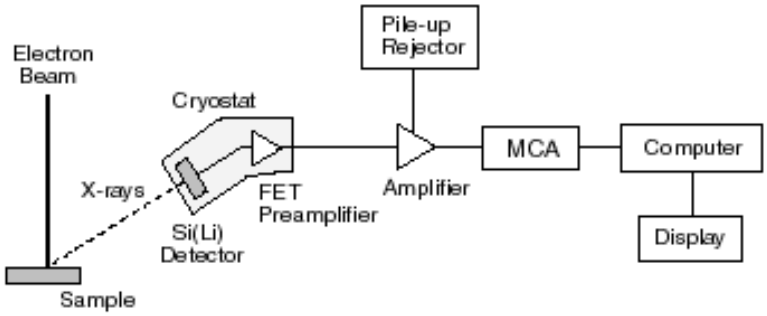

Figure 2.9 Schematic of an EDS [47]

The presence of a protective window to isolate the detector from the chamber has both advantages and disadvantages. First, by keeping the crystal isolated from the microscope chamber, the window prevents condensation of residual water vapour and hydrocarbons from the vacuum that would otherwise contaminate the crystal and affect its efficiency [27, 45]. On the other hand, the window causes loss of x-ray signal through attenuation [48]. Both the thickness and the nature of the window will affect the EDS's detector efficiency. In a conventional EDS, the beryllium window ($\sim 7\mu$m) will absorb all x-rays with energies below 600 eV [27]. The thicker the window is, the more it can absorb x-rays of higher energies, limiting the signal from low Z elements. Thin Be crystal are however very expensive to produce, and it is therefore common to see 12-25 μm windows in conventional EDSs that have very limited capabilities below sodium (Z=11) [45]. A lot of progress has been done however in the last 40 years to overcome Be window's limitations regarding x-ray absorption [49]. Ultra-thin windows (UTW) are made out of various types of polymers or sometimes diamond and are significantly thinner (in the hundreds of nanometers). Polymer windows will allow detection of x-rays down to 100 eV [50]. Table 2.1 summarizes the capabilities of various commercial windows regarding x-rays of low energy from Be to Na). This table allows the following observation : *different window materials absorb light-element x-rays differently* [45].

This means that the detector itself may prevent observation of a particular element in a sample, fact that needs to be considered for sound quantitative and qualitative analysis.

Table 2.1 Transmission of available thin windows for Si(Li) detectors Reproduced from [51]

Window	Area	Be $K\alpha$	B $K\alpha$	C $K\alpha$	N $K\alpha$	O $K\alpha$	F $K\alpha$	Na $K\alpha$
AP1	100 mm^2	7%	24%	58%	39%	52%	61%	71 %
Polyimide	100 mm^2	10%	27%	61%	38%	57%	75%	78 %
BN	30 mm^2	9%	26%	20%	36%	42%	58%	74 %
Si_3N_4	30 mm^2	-	1%	15%	43%	41%	61%	90 %
Be ($5\mu m$)	28 mm^2	-	-	-	-	3%	18%	61 %
Diamond	28 mm^2	4%	14%	36%	3%	13%	29%	51 %

The Li K x-ray line, with an energy of 55 eV, will not be detected by a conventional detector (with a window), which represents a major problem for battery related applications, since lithium is often the key element to understanding electrochemical processes as a result of cycling. A windowless detector is therefore needed for light element x-ray analysis. Windowless detectors are designed so that no absorption of characteristic x-rays occurs since no window is used to separate the detector from the chamber. To avoid contamination in this case, the detector is retracted at all times between uses and separated from the chamber by an isolation valve.

Table 2.2 Signal improvements in a windowless EDS detector versus conventional EDS detector with polymer window. Reproduced from [52]

	Si Ll	Be $K\alpha$	N $K\alpha$	O $K\alpha$	Si $K\alpha$	Mn $K\alpha$
Improvement	x 8	x 3.3	x 2.8	x 2.1	x 1.5	x 1.4

Energy resolution

The energy resolution of the commercial EDS spectrometer is by convention calculated using the full-width at half-maximum (FWHM) of the Mn K_α x-ray line, which stands around 130 eV [27]. Since the Li energy x-ray line is about 55 eV this means a conventional EDS might have difficulties distinguishing the Li K peak from the continuous x-ray background. Recently, a windowless EDS design by Oxford Instruments maximized detection of low energy x-rays, reaching a high of 45eV for energy resolution of carbon and detection of light elements

down to lithium (Z=3) [48].

2.3.2 Quantitative analysis

Castaing (1951) determined that the relative intensity of an x-ray line is related to that element's mass fraction in the analyzed sample. Therefore, comparing the measured intensity of an element i in a sample (I_i) with the intensity retrieved from the measurement of a standard made of that pure element ($I_{(i)}$) will give the approximate mass concentration of i in the sample as shown in equation (2.3).

$$k_i = \frac{C_i}{C_(i)} = \frac{I_i}{I_{(i)}} \text{ [53]} \tag{2.3}$$

However, this first approximation was latter found inaccurate since atomic number, absorption and fluorescence effects contribute to reduce the measured intensity by the EDS detector. Therefore, a correction factor for these matrix effects has to be applied to equation (2.3) in order to correct the x-ray intensities measured and determine the representative elemental mass concentrations in samples.

$$k_i = [ZAF]_i \cdot \frac{C_i}{C_{(i)}} = [ZAF]_i \cdot \frac{I_i}{I_{(i)}} \tag{2.4}$$

The ZAF correction coefficient is divided in three main parts, the atomic number effect Z_i, the absorption effect A_i and the fluorescence effect F_i. All three coefficients are determined using physical models or fundamental equations. The atomic number correction factor Z_i considers the effect of backscattering electrons, which decreases the number of possible x-rays produced when exiting the sample because of high angle scattering, and energy loss in the material. The absorption coefficient A_i takes into account that the number of x-rays detected is greatly reduced from the number that is generated in the sample because of the travel length of the x-rays in the material. Some x-rays will be absorbed in the sample and will not get to the detector. Absorption is the most important correction factor. Finally, many of the x-rays generated will be absorbed by photoelectric effect in the specimen and lead to additional characteristic x-ray generation. This fluorescence effect is taken into account in the F_i correction factor.

The Cliff & Lorimer method [54], based on Castaing's observations, was invented to simplify quantification in thin specimens. Using the thin foil criterion, when absorption and fluorescence effects become negligible, one can achieve quantification by calculating sensitivity factors k_{A-B}, which are independent from the conditions of analysis. The advantage of this technique comes from the fact that no standard is needed to proceed to quantitative analysis of a specimen. The k_{A-B} factors are calculated from the ratio of intensities of two elements (A B) in a binary system. In bulk specimen, standardless analysis which is less time consuming can be achieved by the f-ratio method, developed by Horny et. al [55], which is an alternative to the ZAF correction method that implies knowledge of the experiment conditions (probe current) and is based a ratio of intensities and the Cliff & Lorimer ratio. The advantage of the f-ratio method lies in its smaller error compared to the ratio of intensities of elements used in the ZAF correction method [56].

In order to conduct quantitative analysis of a sample with EDS, a qualitative analysis of recognition must be made beforehand. By identifying the elements present in the specimen, the operator can choose the appropriate standards, and proceed to measurements of both the standards and specimen. Afterwards, mass concentration calculations (C_i) are calculated with equation (2.4) using both the specimen and the standards x-rays spectrums as inputs in a designated software. Standardless quantitative analysis can also be done, in this case the measured specimen x-ray spectrum will be compared with a database of standards. Quantitative analysis with EDS is said to have an *analytical precision and accuracy at the ±1–2% level* [27] .

2.3.3 Difficulties of EDS measurements regarding lithium

Even with a windowless EDS detector, lithium detection in a SEM faces some difficulties. The detector's electronics have to be optimized in order to deconvolute the Li Kα peak from the noise peak [52]. Also, being one of the lightest elements, lithium's fluorescence yield is of the order of 10^{-4} [57] which means that for every 10 000 ionizations of the lithium's atoms in

a materials, only one x-ray will be produced. Therefore, to conduct EDS elemental analysis one has to take into account the very low signal produced by the electron beam. Often even with a windowless EDS detector the counts of Li K x-rays is too low to conclude accurate quantitative analysis. To obtain a 1% relative precision, at least 40 000 counts must be collected in order for the statistical error in an acquisition to be 2σ [58]. In order to increase the x-ray signal, increasing the beam current is generally the accepted solution. However, light elements, especially lithium are known to be highly sensitive to electron beam, which means that the samples will be damaged by the electron beam and lithium can even be sputtered from the material [59, 60], impeding the analysis.

Not only knock-on damage can damage lithium, it is also very sensitive to contamination. Lithium, being an alkali metal, reacts rapidly with oxygen, air and liquid nitrogen as well as water vapour. Following fabrication of lithium metal samples, a passivation layer will almost instantly form on the exposed surfaces, preventing further oxidation. Lithium will therefore oxidize in HV environment. UHV is necessary to study pure lithium, although samples almost always suffer from contamination from the preparation process.

Finally, even if all of these problems were solved, lithium x-ray detection is made very difficult because of very high mass absorption coefficient in the matter and complex emission process. The electronic structure of lithium, with its single valence electron, makes x-ray generation complex in compounds since the same electron that would generate the x-ray is also involved in the chemical bonding with the material. If lithium atoms are bounded in the material, its K shell electron might be trapped and therefore its detection by the ESD might be impossible [61,62]. It has been demonstrated that both theoretical simulations and experimental results renders different yields of x-rays depending on the chemistry and the weight fraction of lithium in a compound, as shown in table 2.3 [62].

Table 2.3 Li K X-ray intensity in binary compounds. Reproduced from [62]

Compound formulae	Amount of Li (wt%)	Experimental (cps/nA/sr)	MC Simulations (x100 cps/nA/sr)	Experimental Li K /Li K^0	MC Simulations Li K /Li K^0
Li (extruded film) (5kV)	100	9697	5458	1	1.00
LiH (5kV)	87.3	2400	2647	0.25	0.48
Li_3N (5kV)	59.8	3125	623	0.33	0.11
L_2S (5kV)	30.2	3500	1665	0.37	0.30
LiF (2kV)	26.8	8458	264	0.88	0.05
LiCl (5kV)	16.4	128	790	0.01	0.14

2.4 EELS & its quantitative analysis

Electron energy-loss spectroscopy, as its names indicates, is a technique that measures the energy loss of electrons as a result of interactions with the sample. Specimen-beam interactions that lead to energy loss are a result of inelastic scattering and lead to ionization of the material's atoms. As mentioned in the previous section, both Auger electrons and x-rays result of ionization events. EELS signal is therefore not limited by the fluorescence yield of the material, since both relaxation phenomenons can be measured in the spectra. The combination of EELS spectrometer with TEM or STEM with spherical aberration correction (C_s) permits sub-nanometer chemical analysis of materials. Compared to EDS, EELS offers also better analytical sensitivity since the solid angle of collection of 4π permits high signal collection [45].

The spectrometer collects all electrons that have gone through the specimen to construct a histogram of the energy distribution. The spectrum can then be interpreted and quantified or used to produce images with specific elemental or chemical information. The spectrum presents therefore various informations about the specimen under study. First, many electrons will go through the specimen without scattering and form the Zero-Loss peak (ZLP). This gaussian shaped peak gives information about the energy resolution of the spectrometer. It is defined by the full width at half maximum (FWHM) of the ZLP. The ZLP is usually the most intense feature of the EELS spectrum, provided the specimen is thin enough. Plasmon peaks are the next most important features in terms of intensity. Plasmons are by defini-

tion oscillations of the free electron gas and as such they are more prominent phenomena in metals. Thick samples will exhibit harmonics of the plasmon energy of the material in the low-loss region (E<50 eV) of the spectrum. In the high-loss region of the spectra (E>50 eV) the elemental and chemical information of the specimen are found, in relatively low intensity compared to the background signal. Ionization edges are directly related to the inelastic scattering of primary beam electron with the electronic shells of the samples atoms. When an ionization event occurs, the primary beam electron looses the energy equivalent to the critical ionization energy of the shell it interacted with. Due to the high energy resolution of the apparatus, fines structures related to differences in valence or bonding states can be seen on the edges themselves. This permits further chemical speciation of the sample under observation. As figure 2.10 shows, plasmon peaks resulting from thick specimen will overlap ionization edges and the fine structure information.

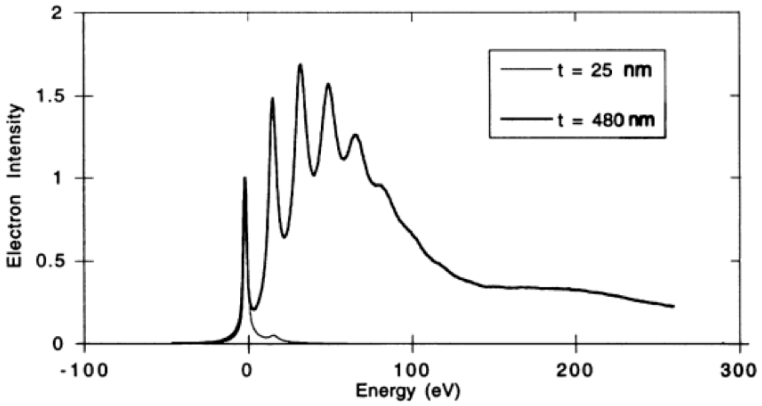

Figure 2.10 Effect of thickness on EELS spectrum [63]

2.4.1 Components

EELS data is collected by a spectrometer below the specimen in the microscope chamber. Figure 2.11 presents a schematic of the apparatus. Upon their exit of the specimen, the electrons enter the spectrometer by the angle-limited entrance aperture and enter a magnetic prism. The field in the prism applies a Lorentz force on the electrons as they travel in a drift tube through the prism. According to their velocities, which are a function of their remaining energy, the electrons will be more or less deviated from their course by the Lorentz

force before impinging on the dispersion plane or camera detector. Electrons that have lost the least energy (that will form the ZLP) are less deviated and impinge on the detector at the bottom of the distribution. Electrons that have suffered higher energy losses will be deviated at higher angles and form peaks at the top of the distribution [63]. A spectrum is thus formed.

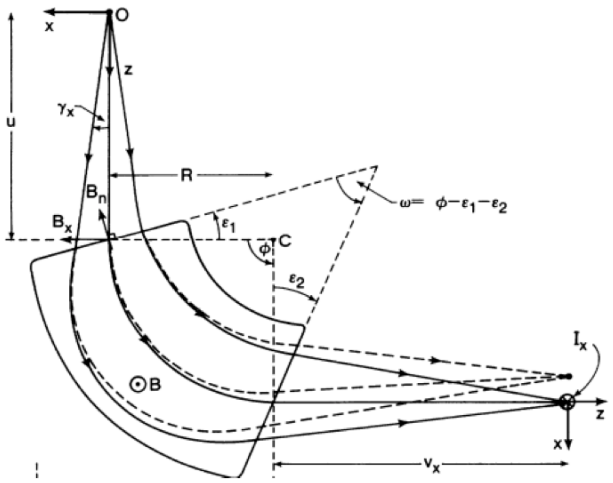

Figure 2.11 A typical EELS apparatus with 90° deflection angle [63]

Energy resolution

Cold Field Emission electron guns (CFE) have the advantage of small energy spread (ΔE). Typical energy resolution for EELS analysis is 1eV [45], although some instruments may offer sub-eV resolution. Chromatic sources will cause broadening of the ZLP and therefore loss of resolution.

2.4.2 Quantitative analysis

The biggest challenge in EELS quantification assuming single scattering is correctly subtracting the background to isolate the chemical information in the edges. A power law function is used to model background intensity in the spectrum [63, 64]. However, it can be difficult to prepare samples thin enough to produce only single scattering events, therefore it is common to observe EELS spectrums with contributions from plural scattering. In these situations, it will be necessary to deconvolute the signal to extract the edge intensity from the plural

scattering artefacts of the low-loss region. The typical method to do so is to use Fourier-log deconvolution, which is explained in details in Egerton's book [65].

2.4.3 Difficulties of EELS regarding lithium

As for EDS, EELS analysis suffers from the high reactivity of lithium in the environment and from its high sensitivity to the electron beam. Lithium being one of the lightest atoms, it has small scattering probability [66] and therefore low signal is obtained. High knock-on probability impedes the analysis and prevents from using high electron doses.

For EELS analysis to give information about a sample's nature and bonding states, the ionization edges have to be separated from plasmon peaks. As mentioned before, harmonics of the plasmon peak can be seen in the spectra and can overlap or even hide smaller analytical signal. Therefore, EELS samples must respond to the thickness criterion :

$$\frac{t}{\lambda} \sim 1$$

Where t is the thickness of the sample and λ the inelastic mean free path of electrons in the sample. This criterion ensures only single scattering events occur in the materials, therefore the related plasmon peak doesn't interfere with edges.

Finally, transition metals have their M edges energy very close to the K edge of lithium, which can make the detection of lithium challenging, due to partial or total overlapping or shadowing of the edges [67, 68]. Since most cathode materials imply the use of transition metals, such as in LFP, LTO, lithium cobalt oxide (LCO), and NMC etc..., analysis of these materials with EELS in search for lithium information can be difficult.

2.5 SIMS & its quantitative analysis

Secondary ion mass spectrometry (SIMS) is an analytical technique in which ionization of chemical species is made by bombardment of a sample's surface with an ion beam and results in the emission of secondary ions along with other sputtered particles. The secondary ions

are collected by a mass spectrometer and analyzed in regards to their mass-to-charge ratio (m/z). The sorted ions are then sent to a counting device (a detector) who displays data in the form of a histogram of the abundance of a chemical species (intensity of ion received at the detector) versus m/z ratio. The y-axis represents the relative abundance of the chemical species in the sample, often it will be normalized with the base peak - the peak of highest intensity. The whole system is kept under vacuum in order for all the incoming beam ions to get to the sample, without collisions lost due to air particles.

SIMS is a destructive method. The primary beam ions will be implanted in the material after high energetic collisions creates a collision cascade in the material, leading to some of the sample's atoms or molecules to recoil back to the surface and be emitted following ionization. Therefore, the surface of the sample is slowly sputtered away by the ion beam. The choice of the sputter rate of the ion beam allows two modes of analysis for SIMS, each giving very different information about the specimen in question. Static SIMS, which implies slow sputter rates, allows for minimal destruction of the top monolayer of the specimen. It is achieved with a low beam energy which allows good depth resolution while ensuring minimal penetration of primary ions in the sample [6]. In this mode, the primary ion dose is limited in order that each primary ion statistically hits a fresh area. It gives surface composition of the sample in order to proceed to its qualitative characterization. Dynamic mode can achieve quantitative analysis of the sample by using high sputter rates, which assures high counts rate of each elemental or molecular species. High sputter rates are established using high energies and a large analysis area, which yields best detection limits because of higher statistics. Three dimensional and depth analysis can also be achieved because the high energy allows in-depth destruction of the sample. In this research, dynamic SIMS will be used for its quantification purposes on lithium high energy batteries.

SIMS is mainly used for trace element analysis in solid materials. Its strength comes from its high sensitivity, high detection limit and high imaging resolution for all elements and isotopes. It is widely used in semiconductor and thin film industries to monitor for dopants and impurities with *ppm* to *ppb* sensitivity. Other applications include composition anal-

ysis of electronics and bulk analysis of light elements in Si matrices. Amongst its other advantages, it offers no need for complex sample preparation, a rapid multi-element analysis and surface or three dimensional analysis as well as possible quantification with standards.

2.5.1 Types of data

SIMS analysis procures the operator three types of data on a sample. The first one, mass spectra, which were explained earlier, consist plots of secondary ion intensity versus the m/z ratio of the elements or molecules present in the analysis volume of the sample. Depending on the mass resolution of the instrument itself, it can distinguish isotopes of elements as well as mass interferences, which consist of two species of identical m/z ratio whose atomic masses differ. The mass resolution $m/\Delta m$ of the SIMS apparatus is therefore important. By definition, it is the mass of interest (nominal mass) divided by the difference between the two species with interfering masses [6].

Depth profiles are graphs showing the intensity of the secondary ions collected in the detector for each analysis cycle of the acquisition. The intensities are therefore a function of the experiment time, which can be related to different depths in the sample since the beam is etching a layer of the surface each time it passes a location on the analysis area.

Finally, secondary ions (SI) image allows one to see the lateral distribution of the species of interest in the sample analysis region. Ion imaging requires a detector capable of keeping memory of where the secondary ions originate in the region of analysis of the sample. Collecting images of the distribution of ions for each depth in the material (each cycle of the acquisition) allows three dimensional analysis of the specimen.

2.5.2 Types of mass analyzers

SI mass spectrometry implies the use of a primary ion beam - often FIB - and the need for a device capable of sorting the secondary ions following their nominal masses (m/z). To

accomplish this task, three types of mass analyzers have been used in history : magnetic sector analyzers, quadrupole analyzers and time-of-flight analyzers. In this section, the three will be compared following the different capabilities they offer.

A quadrupole mass analyzer uses electric fields to separate the ions in order to produce a mass spectrum. The apparatus consists of four cylindrical rods to which direct current (DC) and radio-frequency (RF) voltages are applied. The ions travels in between the quadruple rods to the detector. For a given set of applied DC and RF voltages, a quadrupole field will be created between the cylindrical rods, which will determine which specific m/z ion can be transmitted through the tube, upon undergoing oscillations that will lead to a stable trajectory in the center of the rods. All other ions with different nominal masses (m/z) will be deviated by the electric field and collide in the rods [6]. Since only ions with a specific mass are transmitted at a time, acquisition of a mass spectrum over a wide range of m/z involves multiple measurements of the sample with different values of the voltages applied. The mass spectrum is constructed by scanning of the voltage, allowing for one element (one specific m/z ratio) to be transmitted through the analyzer at a time. The quadrupole acting as a mass filter, few atoms are detected compared to the number of sputtered ions from the sample. Therefore, it is often paired with an electron multiplier which will allow higher sensitivity and higher gain.

A magnetic sector analyzer relies on magnetic fields to discriminate one ion from another. The spectrometer usually consists of an electrostatic sector positioned in series with a magnetic sector. Upon entrance in the analyzer, the ions first go through a slit and then enter the electrostatic sector. The later consists of two plates curved in the form of an arc to which equal and opposite potentials are applied. The electric field created in the vicinity of the plates deflects the ions, according to their kinetic energies. The selected plate potential allows focussing of ions with a particular value of kinetic energy, while the others are dispersed. Afterwards, the remaining focused ions will go through a magnetic sector which will separate the ions according to their mass-to-charge ratio. An exit slit selects which doubly focused ions are detected. Therefore, the magnetic sector analyzer allows a sequential construction

of mass spectra. Varying the magnetic field strength in the second sector will permit ions with different m/z ratio to be focused on the detector by passing through the exit slit. Adjustments of the entrance and exit slits can modify the mass resolution of the instrument.

Finally, a Time-of-flight (TOF) analyzer accelerates the ions inside the device and makes them drift through a known distance, allowing lighter ions to reach a detector faster than heavier ones. Ions are then associated to their nature (m/z) by their drift time, knowing that flight time of the ions is proportional to the square root of mass. All the ions that pass through the analyzer will get, in time, to the detector. Therefore, the complete composition of the material can be acquired in a single measurement.

Table 2.4 shows traditional specifications of the three types of instruments described above.

Table 2.4 Comparison of mass analyzers [6]

Type	Resolution	Mass range	Transmission	Mass detection	Relative sensitivity
Quadrupole	<1000	<1000	0.01-0.1	sequential	1
Magnetic	10 000	>1000	0.1-0.5	sequential	50
Time-of-Flight	10 000	>1000	0.5-0.9	parallel	10 000

For research applications, parallel detection of all elements, high sensitivity and enhanced transmission makes the TOF the best suited analyzer. For such purposes, where the composition of the sample or its distribution is not always known, it is important to get a realistic overview of the material. Section 2.5.7 explains in more details the principles of the TOF analyzer and describes how quantitative measurement can be achieved with it.

2.5.3 Quantitative analysis

In the same way EDS analysis can be used for qualitative analysis, SIMS measurements can help one understand the composition of a specimen. Obtaining quantitative information of the identified elements is essential. However, according to Stevie (2016), SIMS *is not self-quantitative and requires secondary standards* because of the different secondary ion yields of

elements in their chemical environment [6].

The secondary ion yield (Y) is by definition the fraction of sputtered atoms that are ionized by the primary ion beam. Both positive ions and negative ions can be created by the primary ions and their relative ionization potential (or electron affinity for negative ions) are directly related to their secondary ion yield. Y varies over several orders of magnitude over the periodic table [6].

Many other factors affect the secondary ion yield. Bonding of the element to be ionized with its surrounding environment - or matrix - is a critical factor in the determination of Y. An element i in a given matrix can react very differently in comparison to that same element placed in another material. Furthermore, some specific reactive species in the specimen, as oxygen, will enhance the value of Y [6]. This effect is called the matrix effect and will be explained in details later on. Finally, the angle of incidence of the primary beam on the sample is another factor in secondary yield variation.

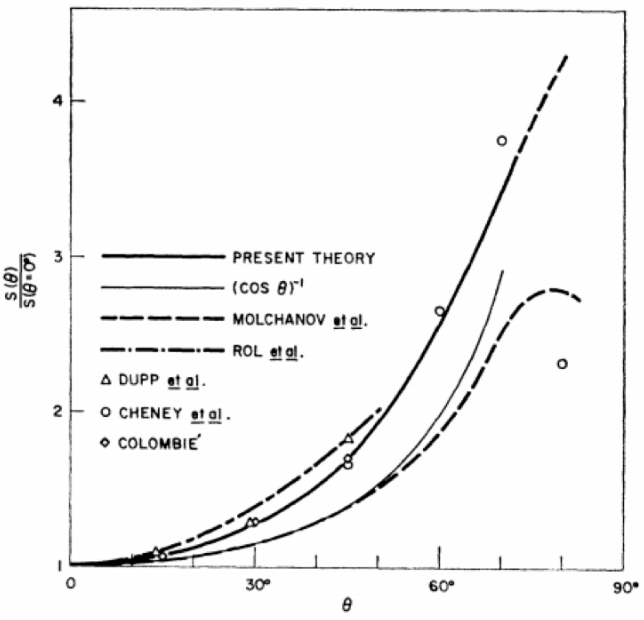

Figure 2.12 Variation of secondary ion yield with incidence angle [69]. Example shown Ar^+ primary ions impinging on copper matrix.

Without correction of the intensities recorded with SIMS, one can only assess semi-quantitative analysis of samples and conduct relative comparisons between them. The best way that has been found to conduct quantitative analysis and to get around the secondary ion yield problem was to measure relative sensitivity factors (RSFs) on standards close in composition to

the specimen and apply this correction factor to the measured intensities of the specimen.

RSFs are by definition functions of a specific element in a specific matrix under a specific primary ion beam bombardment. Therefore, separate RSFs must be calculated for every element in a particular matrix, because the ion yield of the elements vary depending on the matrix as explained earlier. The main utility of RSF is scaling the peak intensity obtained by SIMS acquisition so that they reflect the true sample composition. A high RSF means the analyte element is very insensitive to the primary ion beam and vice versa. Figure 2.13 shows typical values of RSFs under oxygen bombardment. Lithium has the lowest recorded RSF which means its sensitivity is the highest.

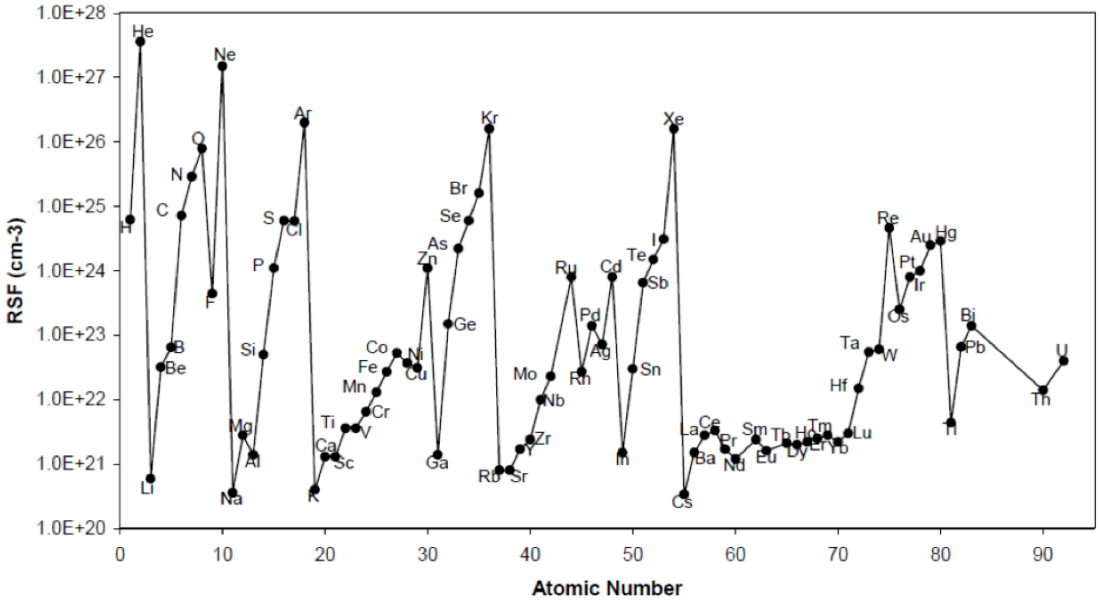

Figure 2.13 RSF for elements Z=3 to 92 implanted into a silicon matrix for O_2^+ bombardment at 8 keV [70]

RSF's main utility is to convert the intensity collected into a concentration of an element i in a material, according to [6] :

$$C_i[atoms/cm^3] = RSF_i \cdot \frac{I_i}{I_{tot}} \tag{2.5}$$

RSF units are $atoms/cm^3$ and it can be computed from the SIMS acquisition according to the following equation:

$$RSF = \frac{D \cdot C \cdot I_m \cdot t}{Z \cdot I_s} \tag{2.6}$$

In this formula, D is the implanted ion dose over all the analyzed region of the sample. It corresponds to :

$$D = \frac{I \cdot T \cdot R^2}{eA} \tag{2.7}$$

where I is the ion milling current, T the dwell time, R the number of locations the beam stops in the analysis region (which corresponds to the number of pixels of the image), e the elementary charge and A the analysis area. The dose is expressed in ions per unit area. In equation (2.6), C corresponds to the number of cycles of the entire analysis, t the time per cycle and Z the depth of the etched crater formed by the analysis in cm. Finally, I_m represents the matrix total secondary ion count rate in cps while I_s corresponds to total counts of the species of interest.

Ion implants

One way to accurately achieve SIMS quantification of a specimen is to use ion implanted standards. To accomplish this task, one has to know the species of interests that are required for quantification and the nature of the specimen matrix. Once these two informations are assembled, the standard can be made. Ions of the species of interest will be implanted with a known dose in the reference matrix, in order to compute the RSF of that element in the matrix. By doing this, the effects of the chemical environment will be accounted for in the RSF and then the concentration determined by measurement on the sample. It is important for the standard matrix to be very close in composition with the specimen to represent accurately the matrix effects.

Because secondary ion yield for alkali elements are known to be high [71], Stevie suggests to attempt its characterization in silicon matrix. In most industries, for example semicon-

ductors, RSFs will be calculated using a silicon matrix since this material is well known, in addition to being a simple, homogeneous structure. In his work, Stevie achieved quantification for Li, K and Na elements in a triple implanted silicon matrix with a detection limit of 1x10^{17} atoms/cm^3 [71].

2.5.4 Difficulties of SIMS measurements

2.5.5 Useful yield

Not all sputtered species are in fact ions. As mentioned before, neutrals are also emitted and constitute the main particles sputtered from the crater. Not every atoms of species i where ionized in the sputtering process and therefore the intensity received at the detector is not necessarily representative of the initial sample. The useful yield (Y_u) which is by definition the number of detected atoms on the number of sputtered atoms can be used to correct this effect.

$$Y_u = \frac{Ions\,detected}{Ions\,sputtered} \tag{2.8}$$

The useful yield is therefore equivalent to the detected ratio of the species of interest by the TOF detector. It corresponds to the counts of species i processed through the analyzer relative to this element density in the specimen's material.

Recombination processes

Mass spectra shows the elemental and molecular species contained in the specimen. Ionized atoms escaping the surface of the sample have to travel in the microscope chamber, the transfer optics and then the TOF chamber before getting to the detector. During this travel, possible recombinations of the drifting ions can occur. Therefore, some molecular compounds that find themselves in the mass spectra might not be representative of the sample's composition.

Studies made on inorganic compounds with static SIMS concluded that many cluster ions were formed after or even during ion bombardment by the primary ion beam. Most re-

combination compounds took the form of an oxidized metal M_xO_y with varying y degree of oxidation [72] or metal recombined with hydroxide ion MOH [73]. While analyzing mass spectra and computing RSF factors for analytes of interest in a substrate, one must be aware of these measurement artifacts.

Matrix effects

The matrix effect, which was introduced earlier, is by definition the combined effect of all the components of the material on the measurement. For consequence, a specie of interest will react differently in the material compound than in a sample completely made of that pure element. It will result in loss or increase in the analytical signal by the SIMS detector. In SIMS, it is the secondary ion yield of the element of interest that will be modified according to the matrix.

Matrix effects render comparison between different samples very difficult because the intensity detected in SIMS is function of the chemical bonding of the atom in the matrix, and it can prevent atom extraction by the primary beam ion or enhance it.

Matrix effects are well known in liquid-chromatography mass spectrometry. For biological samples, some methods allow qualitative and quantitative detection of the matrix effects and even correct for it. A standard addition method in which a multiple point calibration curve is extrapolated in order to estimate the analyte's original concentration in the sample exists [74]. However, with solid electrode material no study has been made in order to suppress the matrix effect, but ion implanted standards in matrices of close composition to the specimen can be done to achieve quantification. For research purposes, it can be however tricky to attempt standard making if the material itself is not well known. In order to achieve quantification with TOF-SIMS for Li-ion electrodes, first the dependence of the RSF with lithium weight fraction in the homogenous material must be assessed.

Roughness effect

Sample topography can greatly affect the secondary ion yield of TOF-SIMS measurements. Although flat-surface approximation is used in all theoretical models for analytical interpretation of SIMS data [76] figure 2.12 shows that the sputter yield of secondary particles is greatly affected by the angle of incidence of the primary ion beam. It is maximum when the primary beam impact angle is high and falls to 0 at 90°. Therefore, SIMS intensity counts are very sensitive to sample topography. In fact, a lot of the contrast seen in TOF-SIMS images comes from the topography of the sample and not the composition itself [77]. Edges, grain boundaries and differences in inclination of different region of a sample will lead to variations in an element intensity which in turn will lead to determination of a wrong elemental concentration in the specimen. Indeed, topography effects can be extremely misleading for interpretation and to conduct quantitative analysis. Furthermore, one has to keep in mind that even if an acquisition might have started on a flat-polished surface, ion bombardment by the primary ions roughens the surface along the way [76]. Therefore, real understanding of the etching effect of the primary ion beam is necessary in order to achieve quantification.

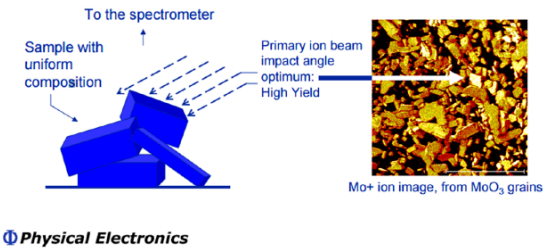

Figure 2.14 Visualization of topography effect on ion detected intensity in TOF-SIMS mapping [75]

2.5.6 Commercial SIMS instruments vs Dedicated SIMS instruments

Many companies offer SIMS instruments. In this section, the advantages and disadvantages of dedicated SIMS versus a portable TOF-SIMS device will be treated.

IONTOF and Physical Electronics both offer on the market TOF-SIMS dedicated analyzers that can reach nanometer scale resolution with a wide range of ion sources. Both optimized ion cluster sources (ex. SF_5, C_{60}), liquid metal ion sources (LMIS) (ex. Ga, Au) as well as Cs^+ and O_2^+ enhancing beams can be used for primary ions. Typically, LMIS and ion cluster sources produce physical sputtering, while Cs^+ and O_2^+ are under a category named chemical

sputtering. The use of the latter reactive species permits more sensitivity and increase of the secondary ion yields by up to two orders of magnitude [78, 79] which is a result of the bond breaking mechanism (O_2^+) or induced change in work function which affects the ionization probability (Cs^+) [80]. Organic materials degrade easily under Cs^+, O_2^+ or Ga^+ bombardment, which is why ion cluster sources (like C_{60} are often used in this field [6, 81, 82]

The IONTOF.5 is a fully polyvalent SIMS instrument with low-noise vacuum system that allows operation in 4 integral mode : surface analysis, imaging, depth profiling and 3D analysis. In surface mode, the instrument uses a finely focused ion beam and can achieve 50 nm lateral resolution with high sensitivity (*ppm*/*ppb* range) and high mass range (up to 10,000 u including molecules without or with little fragmentation). The mass resolution of this instrument is 18 000 ($m/\Delta m$) according to the company's website [83]. The instrument can achieve 1 nm depth resolution in depth profiling mode using a two ion beam profiling. Finally, imaging of regions from the micrometer to the centimeter is possible with up to 10^{15} atoms /cm^3 (or in the *ppb*) detection limit using LMIS.

Physical Electronics' NanoTOFII works using a parallel imaging MS/MS technique. This technique is said obtain *unambiguous molecular fragment ion peak identification and fast parallel imaging* [84] and offers a 70 nm resolution [85]. Using parallel MS/MS technique, 3000 mass resolution (m/Δm) can be achieved with MS^2 [86] with 10ppm accuracy [84].

Cameca's NanoSIMS 50L offer a high resolution magnetic sector mass analyzer with UHV technology with spatial resolution down to 50 nm. It uses reactive ion sources (O^-, Cs^+) which enhances the ionization yield of the sample's atoms by a number of orders of magnitude which increases the total collected signal for each individual atom. The instrument can achieve 3500 mass resolution with 100% transmission efficiency [78]. Being a magnetic sector mass analyzer, the NanoSIMS is limited to 7 masses in parallel acquisition.

TOFWERK offers for its part a Custom TOF-SIMS platform that can be mounted on any equipment with primary ion source to generate secondary ion signal. It can be mounted on

a FIB or FIB-SEM microscope for example, increasing the analytical capabilities of the host instrument. The C-TOF analyzer is a compact detector designed for fast acquisitions and offer a mass range up to 20 000 m/z. The mass resolution of the detector is > 800 m/Δm [87] with a mass accuracy of 4 ppm [88]. The spatial resolution depends on the FIB or FIB-SEM instrument the device is mounted on. Resolution of 50 nm [89] and more recently 40 nm [90] are reported in the literature for TOF-SIMS used with Ga-FIB.

Evaluation

We can evaluate the SIMS devices according to these factors: mass range, mass resolution, acquisition mode and speed, detection limit, vacuum, spatial resolution, compacity and price. High mass range and high mass resolution is especially necessary for organic chemistry, biological samples and applications in pharmaceuticals, were big chains of molecules exists and need to be identified. For battery related applications, lower mass ranges isn't an issue since the materials dealt with do not contain extensive chains of molecules. However, the instrument must be capable of distinguishing Li_2^7 from N^{14}, since lithium is the key element. Although both species have the same nominal mass at 14, their atomic masses are different because the binding energy between the lithium atoms decreases its overall mass (13.882 g/mol versus 14.0067 g/mol for nitrogen [91]). The higher the mass resolution of the instrument, the smallest differences in masses it can distinguish. In this perspective, the resolution needed to distinguish Li_2^7 from N^{14} can be calculated from ratio of nominal mass over the discernible mass difference:

$$\frac{m}{\Delta m} = \frac{14}{m_N - m_{Li_2}} = \frac{14}{0.1247} = 112.27$$

Calculation indicates that even with the lower mass resolution of the above mentioned, TOFWERKS' C-TOF portable detector can single out Li^7 and isotopes.

In terms of acquisition and speed, all TOF-SIMS analyzers permit parallel detection of the all the elements, which is an interesting asset in research where the exact composition of the observed sample might not always be known. The big drawback of the NanoSIMS instrument

for research purposes is the limited (7) parallel mass channels during acquisition, which can enhance greatly the time of acquisition if more than seven masses need to be measured on the sample.

Dedicated SIMS offer greater detection limits, down to *ppb* and generally greater transmission efficiency. UHV vacuum conditions are recommended for adequate surface SIMS analysis but are less stringent in dynamic mode with reactive species where the ion dose is not limited and in depth information is sought [92]. Under poorer vacuum conditions, the residual gas particles can prevent the secondary ions from the sample to enter the mass analyzer, decreasing the detection efficiency of the instrument. Also, the gas molecules have a high sticking coefficient, which means they can attach to the surface and be sputtered with the sample's atoms, impeding the analytical signal perceived in the mass spectra. Dedicated SIMS working under UHV conditions like the NanoSIMS tend to show 100% detection efficiency, while the C-TOF analyzer has reported 20% detection efficiency when combined with FIB-SEM system [79].

Finally, most dedicated instruments offer a maximum of 50 nm resolution. Attaching a C-TOF detector to a FIB column could permit even higher resolutions, although ion sources like Ga source produce limited sputtering yields compared to Cs^+ and O_2^+ [78,79]. The advantage of a portable TOF-SIMS detector comes also from the fact that it is more compact than a dedicated SIMS instrument and the addition on a FIB-SEM microscope allows for a larger scope of analysis on the specimens, for a fraction of the price of a dedicated instrument. For instance, sample imaging is enhanced by the use of traditional SEM signals (SE, BSE) and SE resulting from ionic interaction also render high channeling contrast, while easier navigation through the specimen and in-situ sample preparation (by FIB section for example) is made possible as well as other chemical techniques (EDS) [79, 87]. In this project, the C-TOF detector (TESCAN/TOFWERK AG) mounted on a FIB-SEM microscope (LYRA3, TESCAN) will be used in order to characterize lithium in battery materials since it resolves EDS's detection limitations and the spectra obtained is not affected by other elements interference as in EELS. The FIB allows spatial resolution down to 40 nm. The next section will

describe in more details the principle of TOFWERKS' TOF-SIMS detector.

2.5.7 TESCAN/TOFWERK AG TOF-SIMS detector

Components

The FIB column is the source of primary ions used for a TOF-SIMS acquisition. It sputters Ga ions with energies up to 30 keV towards the sample. A TOF-SIMS acquisition usually consist of a number of repeated cycles in which the ion beam will go through in a given number of locations over a region on the specimen defined by the operator. The number of locations the beam goes through is set by the operator and corresponds to the number of pixels of the resulting image (R). The movement of the beam will cause a crater to widen. The secondary ions that get emitted out of the sample are then collected by the collection optics at a distance of 8 mm from the sample. The collection optics is made of two parts, the extractor and the ion transfer optics. A potential of 20 to 80 V is applied to the extractor, whose role is to attract the charged secondary ions produced by the FIB. Once the ions are engaged in the apparatus, they undergo a post-acceleration of 5 kV. At this point in the instrument, all the ions have the same kinetic energy, so their mass will be the only determinant for their velocities. Light ions will be the fastest while heavier ions will have low velocities and therefore take more time to get to the detector.

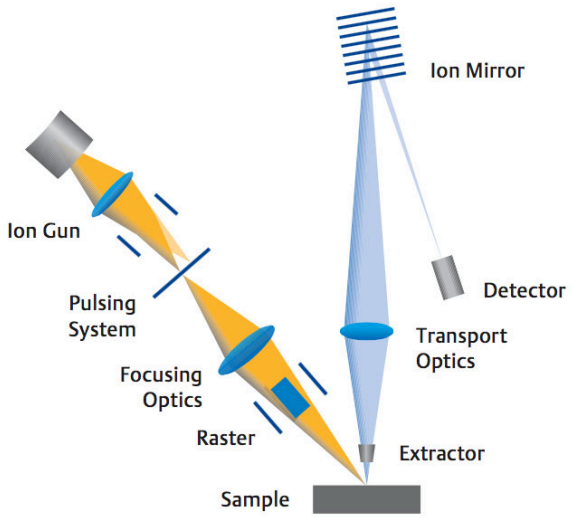

Figure 2.15 Schematic of a TOF-SIMS apparatus [93]

The ions next enter the analyzer tube, which contains the HV pulser, the ion mirror and the SIMS detector itself. The analyzer tube's main function if to provide a drift length for the ions to separate in space depending on their velocities. At the entrance, the HV pulser

is synchronized with the dwell time of the FIB at 10 μs/pixel. Therefore, the detector can discriminate the ions that get to its surface by comparing their arrival time and the time since the beginning of the experiment, knowing each 10 μs the FIB changes location on the sample. It will produce a mass spectra for each point in the map. The total acquisition time is therefore the total number of pixels in the images times the number of cycles (frames) the operator chose (R·R·F). Traditionally in TOF-SIMS devices, the beam itself is pulsed in order to minimize charging onto non- or semi-conductive samples and permit their analysis. However, beam bunching leads to larger beam profiles. In order to get increased spatial resolution, the TOF analyzer designed by TESCAN pulses the detector itself [87].

Next, an ion mirror, also called reflectron, is placed at one end of the analyzer tube. It deflects the ions in the opposite direction with an off-axis angle to focus them onto the detector. This ion mirror has the advantage of increasing the path length of the ions without increasing the physical size of the instrument on the microscope. Increasing the path length of the ions increases their drift time, which has the effect of enhancing the resolving power of the instrument by creating a larger temporal distribution between ions of similar m/z [94]. The principle of the ion mirror is quite straightforward. It consists of a series of electrodes evenly spaced to which an electric field is applied. The fields are oriented in the device in order to oppose the acceleration of the incoming ions and create a retarding effect. The ions then emerge of the mirror with reversed velocity, and pursue their travel to the detector. Since all ions obtain the same kinetic energy because of the 5 kV post-acceleration, ions with low m/z ratio will have higher velocities than ions with greater m/z. As they drift through the analyzer tube, the different ions will separate in space. The ion mirror is used as a solution to this separation in space, to make sure that ions of a specific location arrives at the detector in the right interval of time to be associated with the right location on the image.

Desorption will cause some ions of similar m/z ratios to have different initial velocities. Ions with higher kinetic energies will penetrate deeper in the ion mirror, resulting in longer flight paths. Ions with lower kinetic energy will get to the mirror last but will spend less time in the mirror, with a result that both ions will arrive at the detector at the same time and be

accounted for the same species. The reflectron is optimized so the flight time in the drift region equals the flight time in the reflectron [94].

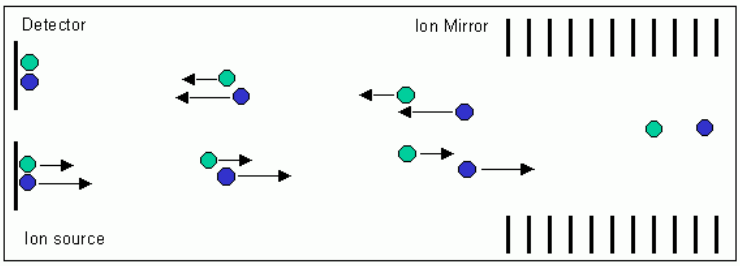

Figure 2.16 Representation of the flight principle in an ion mirror [94]. The blue ion has more kinetic energy than the green ion.

Finally, the ion detector consists of an electron multiplier (EM) which provides high performance with a gain over $\sim 10^8$ [6]. A Time-to-Digital converter (TDC) is combined with the EM processing the ion counts. The TDC senses the pulses sent by the HV pulser, and stores into the computer memory the time intervals between the beginning and end of the voltage pulses. The ions are sorted by their arrival time to the detector. Their nature can be identified using :

$$\frac{m}{z} = \frac{2 \cdot V \cdot t^2}{L^2} \tag{2.9}$$

The observed time-of-flight is the addition of the different steps that ions go through in the TOF-SIMS device and can be expressed as follows [95]:

$$TOF = t_0 + t_{acc} + t_D + t_d \tag{2.10}$$

In equation (2.10), t_0 represents the moment after the beginning of the acquisition (t=0) to which an ion begins to accelerate because of the extractor. t_{acc} is the time it takes an ion to accelerate to its drift velocity, which is induced by the 5 kV post-acceleration of the collection optics. Finally, t_D is the time the ions drifts inside the analyzer tube and t_d the response time of the system.

2.5.8 Applications of TOF-SIMS in battery materials

TOF-SIMS techniques have already been used to characterize battery materials. Mostly, it is used as a qualitative tool for quality control, as traditionaly used in the semiconductor industry, where TOF-SIMS can be used to detect contaminants in cathodes, like iron, coming from the fabrication process and that would otherwise compromise battery safety and performance [96].

For its ability to detect lithium, TOF-SIMS has been also used to investigate the effect of polyethylene glycol (PEG) doping of polypyrrole polymer (PPy) in $LiFePO_4$ (LFP) electrodes, whose principal goal is to increase conductivity of the PPy-LFP cathode and thus improve mechanical and structural properties of the PPy [97, 98]. As it can distinguish organic and inorganic species and molecules, it is an interesting tool to investigate decomposition products implied in the formation of Solid Electrolyte Interface (SEI) [99].

TOF-SIMS's ability to produce depth profiles proved useful in the monitoring of Sn-Co and Sn-Ni alloys as anodes in Li-ion batteries, revealing incomplete initial alloying that resulted in the division of the anode material into two parts : a highly lithiated outer part (Li_xSn) and a non-lithiated inner part [100, 101]. The same studies observed with TOF-SIMS the volume expansion and shrink during discharge or charge and evidenced that those were factors in increasing the SEI layer. Many have used TOF-SIMS to study lithium insertion mechanisms and SEI [102, 103]. ChiHuang et al., stated that iron signal could be used as an index for lithium intercalation in the material, given their same stoichiometry in LFP material. For Bordes et al., fluorine was used as an indicator to determine SEI thickness.

TOF-SIMS was also linked with EDS chemical analysis and microstructure (SEM) in order to investigate Li-related components after electrochemical cycling with the objective of explaining battery performance or degradation effects and lead to better battery design [61]. With the high spatial resolution offered by the FIB, Sui et al. were able to correlate elemental distributions of the cathode's active materials with different state of charge and evaluate the completeness of electrochemical reaction as well as identify ion transport patterns in the

material. The main point of their study was to show that EDS and TOF-SIMS are complementary techniques, since they possess sensitivity for specific elements, and that TOF-SIMS is the key tool in Li distribution analysis because of its high resolution and sensitivity. Figure 2.17 shows Li, Mn and Co mappings of both a fully discharged (top) and fully charged (bottom) samples. The Li mapping on this figure shows that the discharged sample contains "Li hotspots", which consist of areas of Li high intensity. These residual "hotspots" also appear at a full state of charge, revealing that lithium in those regions is being trapped: lithium ions stay immobile. Superimposition of the FIB SE image with the Li maps acquired with TOF-SIMS show that those Li "hotspots" lie along grain boundaries and interfaces with the surrounding matrix. They also attempted elemental quantification of Li, Mn and Co, the active elements, in the cathode, by integrating point by point the element of interest's counts and normalizing with the integrated counts over 100 frames, which rendered the "concentration maps" shown in image 2.17. The mean Li concentration was calculated using the results of the elemental normalized distribution. In their experimental approach, they highlight the fact that edge effects and topography of the material correspond to some regions of high intensity of lithium. However, they offer no insight on how to correct this effect in order to obtain true elemental concentration.

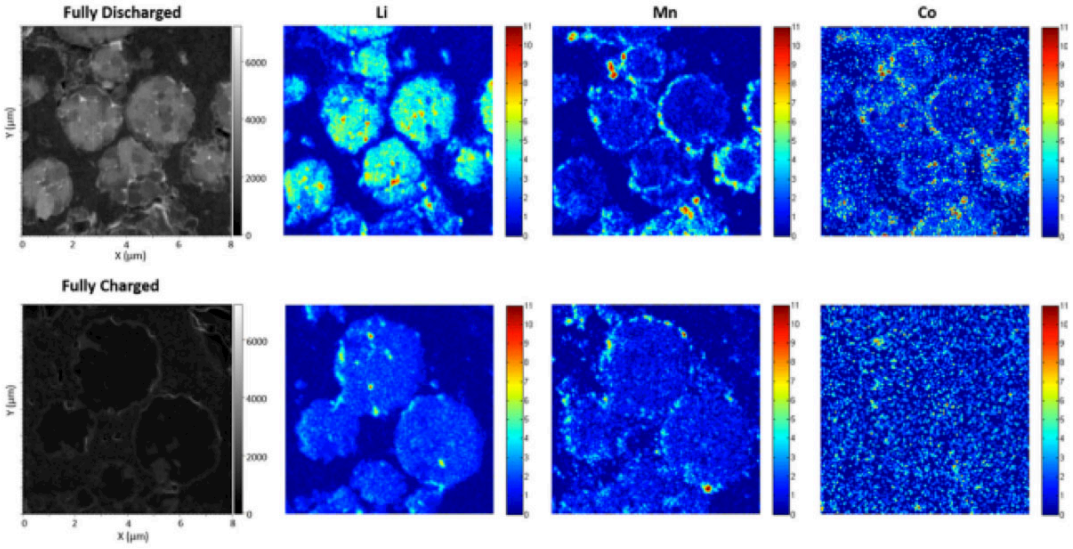

Figure 2.17 FIB-SEM SE images and TOF-SIMS elemental normalized distributions of fully discharged (top) and fully charged (bottom) cathodes [61]

All of these applications show that TOF-SIMS is a proven technology that helps understanding both the physical and chemical properties of battery materials but also provides valuable information on battery behavior and failures during cycling. Its uses and possible applications are vast. Some tried quantification with TOF-SIMS mainly by normalizing the intensities of the peaks of interest by the sum of counts from the rest of the sample's matrix. However, every team who attempted this kind of calculations noted matrix effects and enhanced ion yields with edge or boundaries increased the intensity of elements to values that were not representative of the sample. Although they are aware that these effects affect their concentration determination, none offered a solution to these problems. Adding quantitative results to the experiments detailed above would add valuable information.

CHAPTER 3 METHODOLOGY

In this project, NMC particles are analyzed with TOF-SIMS in order to view Li and active elements (Ni, Mn, Co) ionic distributions within secondary grains. This section will describe sample preparation as well as the characterization techniques used in the following chapter.

3.1 FIB-SEM apparatus

A LYRA3 GT FIB-SEM microscope (TESCAN), shown in figure 3.1, composed of a field emission electron source and Ga^+ liquid metal ion source is used to characterize the microstructure of NMC cathodes. The FIB column is positioned at 55° from the electron gun.

An orthogonal Time-of-Flight Secondary Ion Mass spectrometer resulting of the combined work of TOFWERK AG and TESCAN is mounted on one of the upper ports of the microscope chamber. This portable device allows chemical mapping of the samples under observation as well as chemical identification of the sputtered species (atoms and molecules). Along with the windowless EDS detector (at the back) this TOF-SIMS detector is one of the reasons why this particular FIB-SEM system is unique for battery R & D, allowing complementary techniques for lithium detection.

Samples are tilted 55 ° from the normal to provide normal incidence surface to the ion column during TOF-SIMS analyses (refer back to figure 2.1). Both FIB induced SE imaging and SEM imaging is possible in this configuration.

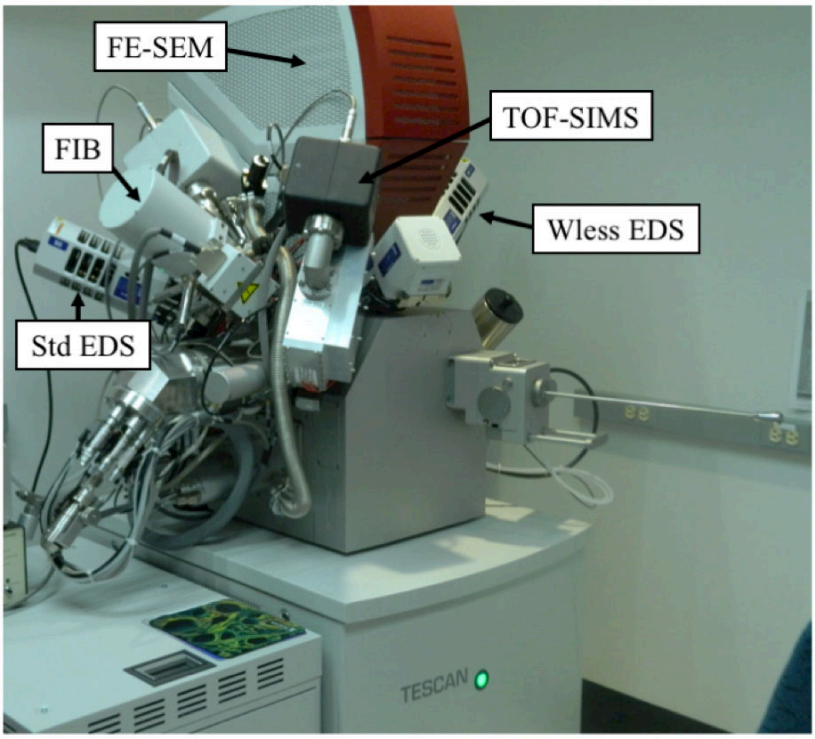

Figure 3.1 Lyra3 GT FIB-SEM used for experiment located at Hydro-Quebec's Research Center (CETEES)

3.2 Sample preparation

Both NMC powder and NMC cathodes were analyzed in this project. The cathodes were prepared in CETEES facility. First a slurry of the NMC powder, along with carbon to improve the cathodes conductivity and finally polymer binder (Polyvinylidene Fluoride or PVDF) is used to ensure adhesion of the elements with themselves and with the current collector. The slurry was prepared in NMP solvent as to allow uniform distribution of the components. The mixed paste was loaded onto a coating machine which spreads the mix onto a metal collector, here aluminium, then dried to evaporate the solvent. The cathode is then assembled in a battery with lithium metal anode and separator and cycled. The methodology for battery assembling and cycling is described in the following chapter. Once the desired cycling state was obtained, the batteries were disassembled and dried before sending to characterization processes.

Cross-sections of both NMC powders and NMC cathodes were used in this project. Cross-sections milling were necessary as to provide a flat surface for TOF-SIMS analysis, subject to edge effects, and because the surface of NMC spheroidal particle lead to increased topography and therefore misleading analyses. Both FIB ion milling and Ion milling with Argon milling system (Hitachi, IM4000+) were investigated.

FIB milling inside the FIB-SEM microscope resulted in flat looking trenches (see figure 3.2) with the use of a protective platinum coating to prevent curtaining of the milled region. However, trench size is limited by the FIB-SEM software to 50 μm width and 40 nm depth. Also, the geometry of the milled trench using FIB obstructs secondary ion path to TOF-SIMS detector, so not all particles milled with FIB can be properly analyzed. Sampling is therefore limited using FIB milling. Assuming a fib trench to take up to four or five hours (using the mentioned size on NMC material), this milling technique is found to be time consuming, especially considering statistical sampling required for sound analysis. On the bright side, the milled surface has a flat appearance and little curtaining is found on the particle.

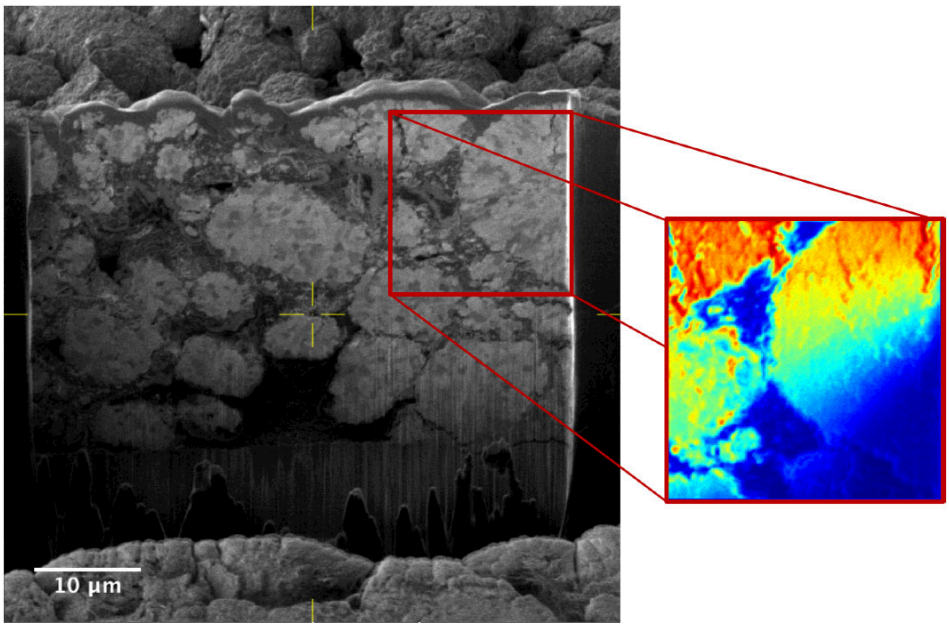

Figure 3.2 FIB SE image of trench made with 30 keV Ga ion beam on NMC cathode sample. Expanded view show Li^+ distribution of the analyzed particle. Decrease in intensity is seen from top of distribution to bottom and bottom right shows shadowing from the trench walls.

Ion beam milling was found to be a less time consuming alternative to FIB milling. Large analysis areas, up to 300 microns and more can be obtained with Ar Ion Milling 4000+ . Both sides of double-sided cathodes can be studied. A large amount of particles is available so statistical sampling of the NMC cathode samples is increased. As an added advantage cross-section milling with Ar beam reduces Ga poisoning of the sample since the FIB ion beam is only used for analysis and not preparation. Optimal milling conditions that rendered 120 nm height differences on NMC cathode particles were found using 6kV beam, 1.5 hours milling under C3 mode (3 reciprocations/min ,±30° swing), with 2 minute flat milling using F5 (15 reciprocations/min ,±60deg swing) and identical energy beam. The flat milling in the end reduces curtaining aspect of the milled sample. For cross section of NMC under powdery form, the particles were first embedded in silver paint to provide a dense, conductive support. The paint was applied on a silica lamellae which was attached to the specimen stub. Similar milling conditions are applied to mill the powder samples.

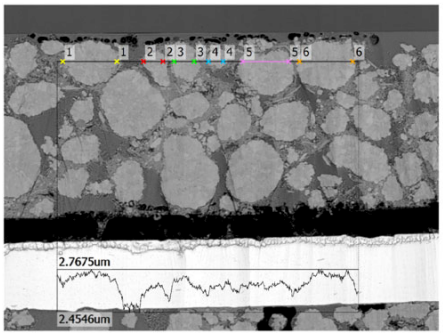

Segment	Height difference (nm)
1	129.1
2	122.8
3	94.5
4	78.7
5	69.3
6	129.1

Figure 3.3 Image of cathode cross section with confocal microscope and related height profile. Height differences were noted on 6 different particles and used to evaluate the sample's milling process

3.3 Sample analysis and data processing

NMC powder was analyzed using laser scattering Particle Size Distribution Analyzer (PSD) (Horiba, Model LA-950). Figure 3.4 shows the obtained particle size distribution. Mean diameter of the particles is 13.20μm . TOF-SIMS analysis region was then set to 15 μm as to incorporate whole particles within one acquisition. X-ray diffraction (XRD) analysis was used to corroborate the lithium content with the cycling data as described in the following

chapter.

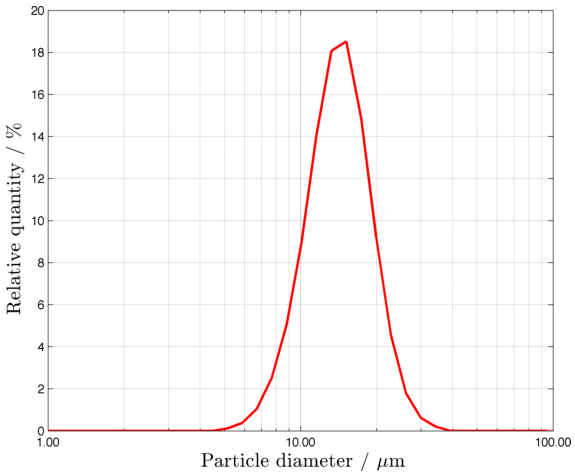

Figure 3.4 Particle size distribution of pristine NMC powder

TOF-SIMS acquisitions were done on pristine and cycled cathode samples. On each sample 10 to 15 region of 15 μm width were selected and the results were averaged to obtain a single point to plot at the related cathode SOC. The NMC samples chosen were disinclined to charging, which rendered the TOF-SIMS analysis successful. Any charging occurring at the sample would have resulted in drifting of the analysis region and poor correlation in ionic distributions. Similar experiments were done in the studies that lead to the results shown in figure 2.17 and no charging was mentioned in that NMC material either.

TOFWERK software allows the selection of regin of interests (ROI) from the total acquisition. Both the ROI's surface and the number of frames the ROI relates to can be modified. This options allows the user to carefully select the parts in the analysis region to pursue further quantitative analysis. The cathodes being mixed with binder and polymer and then dried, the matrix contains numerous pores between NMC particles that act as electrolyte reservoirs, facilitating lithium ion transport. In the post-mortem TOF-SIMS analysis of the cathode, pores appear as regions with poor intensity of lithium and other active elements. Cycled cathodes can suffer from volume expansion during cycling and the particles are subject to cracking. Cracks disrupt the sample's flat topography and appear more intense on the ion map distributions due to enhanced sputtering from non-normal incidence as introduced in

the previous chapter. Figure 3.5 shows the relative difference in lithium ion intensity over a pore, a crack and the matrix background, showing the importance of selective analysis.

To compute TOF-SIMS intensities for NMC that are free from artifacts starting from 15 μm square regions, an extensive number of small ROI's, with 3 to 10 pixels in both x and y direction were selected using the provided TOFWERK data analysis software, by dragging the x and y cursors from the edge of the map to select the desired area. Grayed out regions are then not considered for analysis. A *.txt* file containing in each column data from the complete set of ROIs was exported from the mass spectra panel and incorporated into MATLAB for integration. A homemade script was used to integrate the mass spectra at the elements of interest, namely Li, Mn, Ni and Co over all the analysis regions.

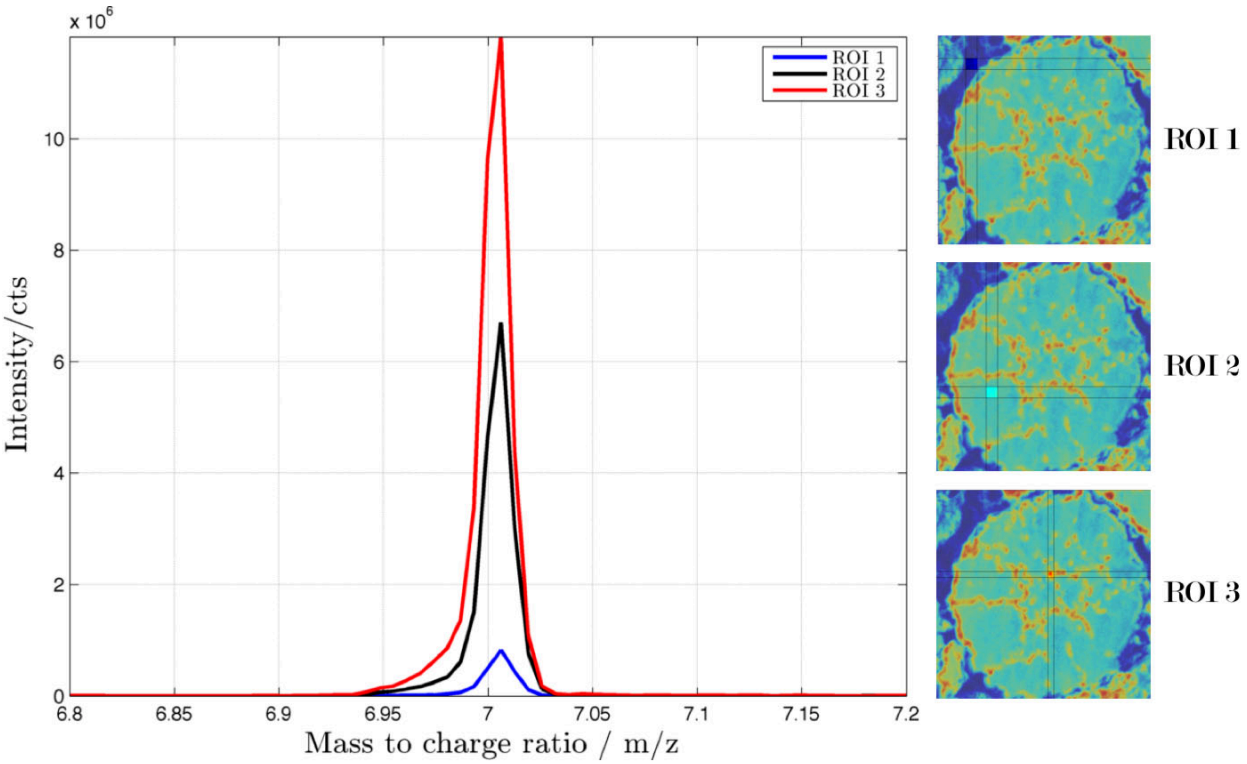

Figure 3.5 Comparison of different features inside Li ion map. Region of interest (ROI) are defined using the x and y cursors over 1) a pore, 2) the NMC particle matrix and 3) a crack inside the NMC particle exhibiting edge effects. Plot shows the difference in lithium ion intensity relative to the selected ROI.

CHAPTER 4 NANOSCALE LITHIUM QUANTIFICATION IN $Li_xNi_yCo_wMn_zO_2$ AS CATHODE FOR RECHARGEABLE BATTERIES

Stéphanie Bessette[1,2], Andrea Paolella[1], Chisu Kim[1], Wen Zhu[1], Pierre Hovington[3], Raynald Gauvin[2] and Karim Zaghib[1,*]

[1] *Hydro-Québec, Center of Excellence in Transportation Electrification and Energy Storage, Varennes, J0L 1N0, Canada*

[2] *McGill University, Department of Mining and Materials Engineering, Montréal, H3A 0C5, Canada*

[3] *Consulting Hovington, Boucherville, Québec, Canada*

*E-mail: Zaghib.Karim@ireq.ca

Preface

Nanoscale Lithium Quantification in $Li_xNi_yCo_wMn_zO_2$ as Cathode for Rechargeable Batteries is a comprehensive work which explores TOF-SIMS in FIB-SEM microscope for battery material applications. This paper has been submitted to Scientific Reports July 19th, 2018 and accepted September 28th, 2018.

4.1 Abstract

Time-of-flight secondary ion mass spectrometry (TOF-SIMS) using a focused ion-beam scanning electron microscope (FIB-SEM) is a promising and economical technique for lithium detection and quantification in battery materials because it overcomes the limitations with detecting low Li content by energy dispersive spectroscopy (EDS). In this work, an experimental calibration curve was produced, which to our best knowledge allowed for the first time, the quantification of lithium in standard nickel manganese cobalt oxide (NMC) cath-

odes using 20 nm resolution. The technique overcomes matrix effects and edges effects that makes quantification complex. This work shows the high potential of TOF-SIMS tool for analytical characterization of battery materials, and demonstrates its tremendous capabilities towards identification of various chemical or electrochemical phenomena in the cathodes via high-resolution ion distributions. Various phenomena in the ion distributions are also assessed, such as edge effects or measurement artifacts from real signal variations.

4.2 Introduction

Scanning electron microscopes (SEM) are essential tools for microstructure characterization and microanalysis of new materials, and their ease of use has made them one of the most widespread tools for analysis of structures down to the nanometer scale [4.1]. Furthermore, the characteristic x-rays from the beam-specimen interactions allow chemical identification of the samples, when observed by an energy-dispersive x-ray spectrometer (EDS) detectors in the microscope chamber. In battery R & D, conventional EDSs are not very useful for detection of lithium (the key element in a battery) because the characteristic x-rays (Li K $\sim$ 55eV) have too low energy, and are absorbed in the instrument window, typically made of beryllium or polymer. Special windowless EDS detectors with optimized electronics [4.2] were developed to permit lithium detection and have proven effective to detect lithium soft x-rays in pure Li-metal and binary compounds [4.2, 4.3]. However, it has been demonstrated that even an optimized windowless EDS has limitations for Li detection and quantification due to its low sensitivity (>20 wt%) and lack of understanding of Li x-ray emission processes [4.3]. In addition, the mass absorption coefficient (MAC) of Li K x-ray within the matter is high, adding to the difficulty to detect lithium. Finally, lithium is a light element with a low fluorescence yield, of the order of 10^{-4} [4.4], which means that electron beam excitation of the lithium core shells results in prevailing relaxation into Auger electrons, therefore the lithium x-ray signal in SEM is very low.

Other alternatives to EDS, which include Electron Energy-Loss Spectroscopy (EELS) and Secondary ion mass spectrometry (SIMS), have limitations for lithium detection. EELS collects the energy distribution of electrons after their passage through a specimen, giving

information about the chemical composition of the sample (ionization edges) and bonding states through edge fine structures. Mounted on a TEM or STEM, an EELS detector is promising for lithium detection in materials since it can detect all energy-loss events, therefore low fluorescence yield of lithium is not a constraint as in EDS. However, electron beam sensitivity is a concern as with EDS analysis. In addition, EELS measurements require adequate thin foil sample preparation, otherwise the lithium K edges can be masked by plasmon peaks [4.5]. Another drawback of EELS for analysis of battery materials is that the $M_{2,3}$ edges of the transition metals used in typical cathode compounds (Mn, Fe, Ni and Co) are very close to the Li K edge, therefore some information about the lithium fine structure can be shadowed by the transition metals [4.6]. It is possible to indirectly analyze lithium in these compounds by correlating the effect of lithium bonding on the change of transition metals and oxygen chemical states and fine structures. SIMS appears to be an adequate solution to the detection limits of EDS, since being a physical sputtering technique, it relies on collision cascades created by energetic ions rather than electronic transitions following excitation of an atom by a primary beam electron. It allows high surface sensitivity, as well as full coverage of the elements in the periodic table, including lithium. Typically dedicated SIMS instruments (TOF-SIMS or magnetic sector analyzers) allow 50 nm resolution along with high mass resolution (>3000) and high sensitivity (ppb) under ultra high vacuum conditions (10^{-9} Torr) [4.7–4.9]. A compact C-TOF SIMS detector by TOFWERKS is available on the market that offers 4 ppm mass accuracy together with sufficient mass resolution (800) to successfully distinguish lithium, transition metals and isotopes. Combining a C-TOF detector in a focused ion-beam scanning electron microscope (FIB-SEM) will allow unique imaging and analysis capabilities of bulk battery samples. In addition, the FIB probe used as ion source allows a higher spatial resolution (40 nm recently reported with Ga FIB [4.10]) than some dedicated SIMS instruments. However, Ga FIB permits commonly 10 nm probe sizes [4.11], TOF-SIMS mounted on a FIB-SEM platform is therefore a *pragmatic, cost-effective*, high-resolution technique in comparison to EELS and dedicated SIMS instruments, although it may not reach the latter's sensitivity (ppb) [4.12, 4.13].

SIMS has been used so far in battery R & D mostly as a qualitative tool. It provides information on the distribution of active materials in $LiCoO_2$ cathodes [4.14], on the effect of polymer

additives on lithium-ion distributions in lithium iron phosphate (LFP) cathodes [4.15, 4.16], permitted study of solid electrolyte interphase (SEI) formation during charge-discharge cycles [4.17, 4.18] and quality control of manufactured electrodes. Furthermore, it is also an important tool to identify lithium-ion hotspots trapped in grain boundaries as a result of battery cycling [4.19]. To the best of our knowledge, the quantification of Li in battery materials and studies of edge effects and matrix effects using TOF-SIMS mounted on a Ga FIB microscope has not been successfully performed.

The edge effects are observed as local variations in signal intensity arising from the change in sputtering yield caused by topography of the sample. The sputtering yield, which is proportional to the intensity in the SIMS spectrum, is an increasing function of the angle of incidence (θ). It has a dependency of $1/cos(\theta)$ from 0 to $\sim 70^\circ$ [4.20], where it is demonstrated experimentally that the function reaches a maximum and falls to 0 at 90° [4.21]. Therefore, edge effects can easily lead to misinterpretation of the content of an element in a sample by showing regions with higher intensities that are artifacts related to the increased sputtering. In semiconductor materials, these edges effects are mainly seen at the edges of the crater formed during SIMS analysis. A simple electronic gating [filter] of the data collected can be used to remove the crater edge effects by sputtering a larger area than the acquisition area [4.22]. Considering that a) battery materials are inhomogeneous and b) the cycling process creates defects in the particles (cracks, pores, etc...), identifying the edge effect is made more complex and this gating technique cannot be applied.

Matrix effects are variations of the yield of secondary ion species in a chemical environment where an element of interest is found. A quantification scheme exists for SIMS analysis, which implies correction of the matrix effects, but is developed and proven for trace elemental analysis, mostly of dopants in homogeneous and simple matrices such as silicon. This scheme needs an implanted secondary standards of known composition to reproduce emission conditions and from which matrix correction factors, so called relative sensitivity factors (or RSF) are computed and used to correct the intensity collected in the SIMS measurement [4.23]. RSFs are specific to the element of interest, the matrix and the ion bombardment under

which the analysis is done. Quantification of matrix levels (by definition more than 1 percent atomic), can be achieved using SIMS, requiring implanted standards of the species of interest [4.23, 4.24]. It has been achieved, to our best knowledge, only with semiconductor-type materials by the study of depth profiles. Battery materials have complex stoichiometry and inhomogeneous structures: it means that a quantitative model must be developed for SIMS since identification of lithium content is of primary importance in this field.

In this work, a Time-of-Flight SIMS (TOF-SIMS) detector (that allows rapid and parallel detection of all elements) was used to quantify, for the first time, Li in standard nickel manganese cobalt oxide (NMC) cathodes. It will be shown that the matrix effects can be assessed by an experimental calibration curve and that edge effects can be understood and distinguished from other phenomenon in ion distributions. The aim of this work is to develop a quantitative technique to be used as a complement to EDS for lithium ions in battery materials.

4.3 Results and Discussion

4.3.1 Matrix effects in NMC

Figure 4.1 shows a typical SIMS spectrum obtained in positive mode at a representative location on a fully lithiated NMC cathode. A strong lithium peak and the presence of nickel, cobalt and manganese are observed, as well as gallium isotopes from the primary ion source. Lithium compounds with transition metals or/and with oxygen in small quantities are also found in the mass spectra (3 orders of magnitude smaller than Li peak) but not identified on the figure. Ni, Co and Mn show smaller intensities compared to lithium, as seen in the expanded view in **Figure 4.1** . These smaller intensities are explained by lithium being in SIMS is one of the most sensitive elements since its low mass and low binding energy gives a high sputtering yield [4.25]. Matrix effects can further emphasize the emission of Li atoms from the NMC compound. In this next section, we will prove that matrix effects in the samples prevent us from direct quantification of lithium in the compound. According to theory, chemical bonding in a material can either prevent or enhance atom extraction compared to the signal received from a pure sample of the element of interest [4.23].

Comparing the SIMS signal with pure lithium metal and the Li signal from NMC in this case proves the existence of matrix effects that emphasize lithium extraction. Under similar bombardment conditions and ion dose, our experiments show that Li intensity is 1.76 times higher in the compound that in the pure material. Using the Transport of Ion in Matter (TRIM) program (part of the Stopping and Range of Ion in Matter (SRIM) software) [4.26] which allows calculation of the sputtering yield of elements in a variety of compounds, we can study the theoretical behavior of lithium emission. From the results in Table 1, we calculate the theoretical emission ratio of lithium in the two matrices and compare it to the ratio of intensities obtained experimentally where the intensity collected in SIMS is directly proportional to the sputtering yield. TRIM renders a theoretical ratio of lithium in the NMC matrix versus in pure Li matrix of 0.76. The theoretical ratio doesn't take into account preferential sputtering, which can cause stoichiometry change in the compound. It is possible that enhancement of sputtering yields in the experimental results is due to surface roughening of the sample over the analysis time [4.27]. The software computes the surface sputtering analysis using a flat, always intact amorphous surface. In our measurement, we took into account regions of interests (ROI) (regions of 10x10 pixels or less) that were free from edge effects, and we stipulate locally that the surface is homogenous. This way, we conclude that matrix effects are occurring in NMC and affect the emitted signal. From **Table 4.1**, it is also observed that the sputtering yield of elements in NMC is inversely proportional to their surface binding energy [4.20]. This fact, and considering that lithium is a light atom in a matrix composed of heavier elements, can contribute to cause the particularly strong sputtering of Li in the NMC compound and adds to the influence of chemistry of the material on the lithium signal intensity.

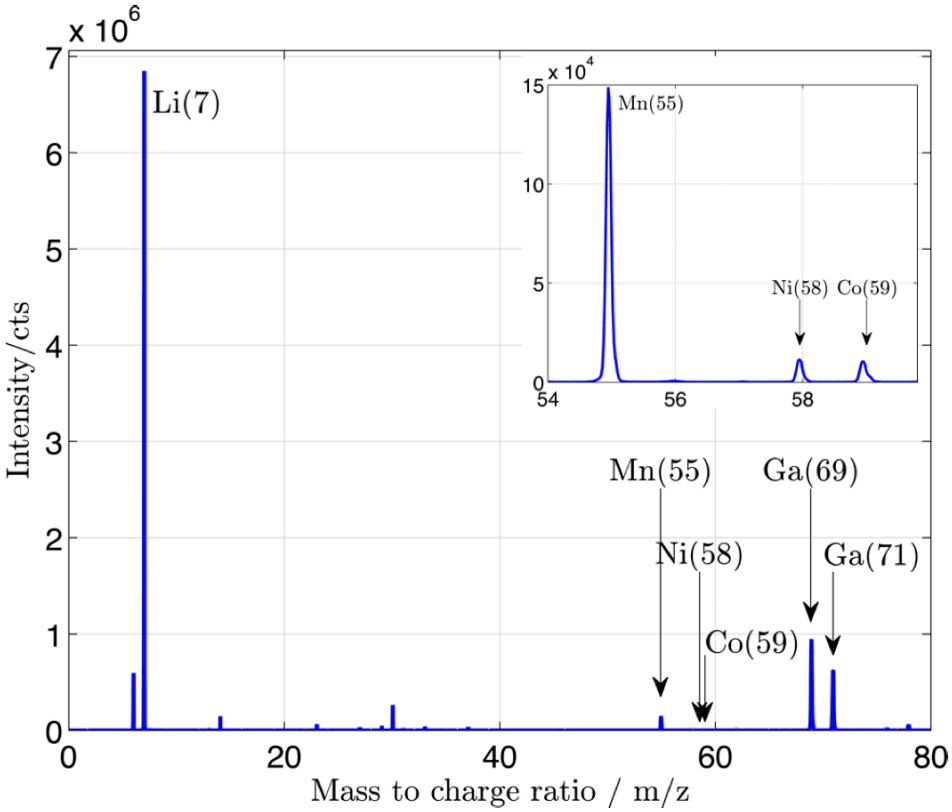

Figure 4.1 Mass spectra of Li in NMC cathode with full lithium intercalation. Identification of Li(7), Mn(55), Ni(58), Co(59) as well as Ga(69) & (71). Expanded view of m/z region from 54 to 60.

Table 4.1 Sputtering yield of Li in pure lithium and Li, Mn, Ni, Co in cathode material calculated by TRIM software [4.26] (using default 99 999 ions in surface sputtering) from Ga^+ bombardment at 30keV

Element	Matrix	Sputter yield (Y) (u.)	Surface Binding Energy (SBE) (eV)
Li	Li	2.2500	1.67
Li	NMC	1.6700	1.67
Ni	NMC	0.4849	4.46
Co	NMC	0.1919	4.43
Mn	NMC	0.3964	2.98

It is clear that Li suffers from matrix effects in NMC compound, and steps must be taken to correct the collected intensities to properly quantify the lithium content in the NMC cathode. As mentioned before, the existing quantification method suggests the determination of RSFs. Computation of these factors imply that the concentration in the reference element

and the standard [4.23] is constant in the sample Usually, the reference element is present in significant concentrations in the specimen sample. This major component happens to be, for example the Si or Ge matrix, and the elements of interest are present only in trace amounts, therefore the reference intensity remains constant. In this case, since lithium is the major constituent and element of interest, another reference must be chosen. The reference should be selected from the other active elements in NMC. However, **Figure 4.2** shows the intensity of Mn, Ni and Co in the cathode at different state of charges (lithium content x in the material). For all of the elements, a net decrease in the intensities was observed as well as a poor statistical correlation. The first phenomena is explained by the fact that intercalation of lithium in the compound affects its chemistry, so Mn, Ni and Co suffer a decrease in mass fraction in the compound as lithium stoichiometry passes from 0 to 1. The absence of a linear correlation in the curves is explained by few collected counts of Mn, Ni, Co, resulting from low sputtering yield as seen in **Table 4.1**. As shown in **Figure 4.1** , it is possible to observe that the lithium peak is an order of magnitude higher than the manganese peak in the compound. In Figure 2, we see that manganese has intensity 10 times higher than both Ni and Co, due to its lower surface binding energy. Ni and Co are neighboring elements in the periodic table, which contributes significantly to the mass effect, with the lighter atoms being ejected preferentially from the surface. Therefore a small variation in the shape of the Mn, Ni, Co peaks on the mass spectrum can lead to a noticeable difference in the integrated intensity. Since the intensity and the concentration of Mn, Ni and Co fluctuate in the compounds, it is not possible to consider them as invariable references in order to determine the concentration of lithium. Finally, another argument that plays against the use of RSFs with our cathodes is that the computation of the RSF correction factor also implies the estimation of the depth of the sputtered crater on the analysis region as a result of destructive sputtering. Taking Si in implanted semiconductor samples as an example, sputtering on this monocrystalline material creates a square uniform crater, and its depth is assessed by SEM imaging of stylus profilometry in the equipment [4.23,4.28]. However, NMC particles are mainly constituted of agglomerated primary particles of ~ 500 nm, and therefore the samples exhibit different and random crystallographic orientations with respect to the primary ion beam. Adjacent grains with different crystallographic orientation suffer from different milling rates [4.29], making the determination of the crater depth impossible since the sputtering technique reveals grains

lying underneath the surface ones, which might be orientated differently.

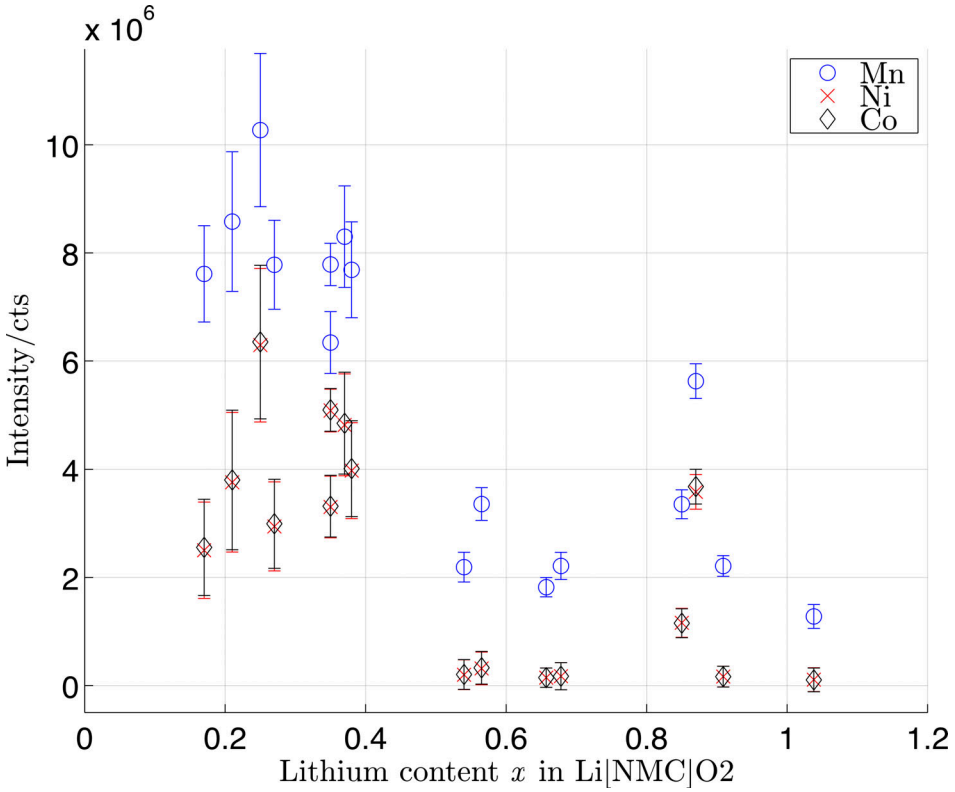

Figure 4.2 Variations of the intensities of the active elements in NMC compound (Mn, Ni, Co) versus the lithium stoichiometry (x of Li) in cathodes electrochemically cycled and at different state of charge.

4.3.2 Calibration curve of Li in NMC

Since the mass spectra is mostly composed of lithium counts and because of failed attempts to compute RSF with the inhomogeneous and complex stoichiometry of NMC, construction of an experimental calibration curve based solely on the experimental lithium intensity was the best option to comply with the nature of battery materials.

Figure 4.3 represents the electrochemical calibration curves under different cycling rates. The y-axis is the measured lithium intensity (in counts) while the x axis is the lithium content (or stoichiometry) in the NMC compound. The amount of lithium (x) in the cathode is inversely proportional to the state-of-charge of the battery; therefore a fully discharged

battery corresponds to a cathode with full lithium intercalation (x=1). To obtain this curve, it should be noted that measurements of the lithium intensity for small regions of interest (ROI) at the surface of grains are not affected by edge effects. The next section will explain how we have distinguished them. For each value on the curve in **Figure 4.3**, an extensive number of acquisitions of 15x15 m regions were taken on each of the NMC samples, and multiple ROIs defined within the analysis areas in order to obtain good statistics. X-ray diffraction analysis of the cycled cathodes was done to confirm the lithium content in the materials (Supplementary Figures **4.6** and **4.7**). Similarly to RSFs, this calibration curve allows the quantification of Li in NMC, with gallium bombardment at 30 keV and 500 pA (analysis conditions). Corrections must be applied for different analysis conditions (different view field, and current) to account for the change in applied dose over the analysis area (higher dose triggers higher sputtering). Therefore, this curve is specific to NMC and to gallium bombardment. Hence, if lithium concentration is to be determined in another battery sample or with another ion source, a new calibration curve must be constructed.

Both electrochemical and chemical delithiation processes have been investigated to assess bulk phase distribution of polycrystalline cathode materials and to help understand the role of the electrolyte on the material [4.30]. In this work, standard NMC powder was chemically delithiated using dibromine as an oxidant, then analyzed with TOF-SIMS under the same conditions as used previously. Three samples were made by using different amounts of the oxidizing agent (ranging from none to in excess) to produce NMC powders with different degrees of lithiation, which are obtained chemically. The powders were then dried and prepared for observation under the microscope without cycling in a battery. The dashed curve in **Figure 4.3** relates to these results. Note that since Br_2 is a mild oxidant (with redox couple 4.01V against Li^+/Li), it cannot delithiate NMC compound further than x=0.5. The chemical delithiated curve for lower lithium content (x) was extrapolated. Both curves are fairly parallel, the difference ΔI represents the added analytical signal of lithium that can be associated to residual lithium from the electrolyte salts.

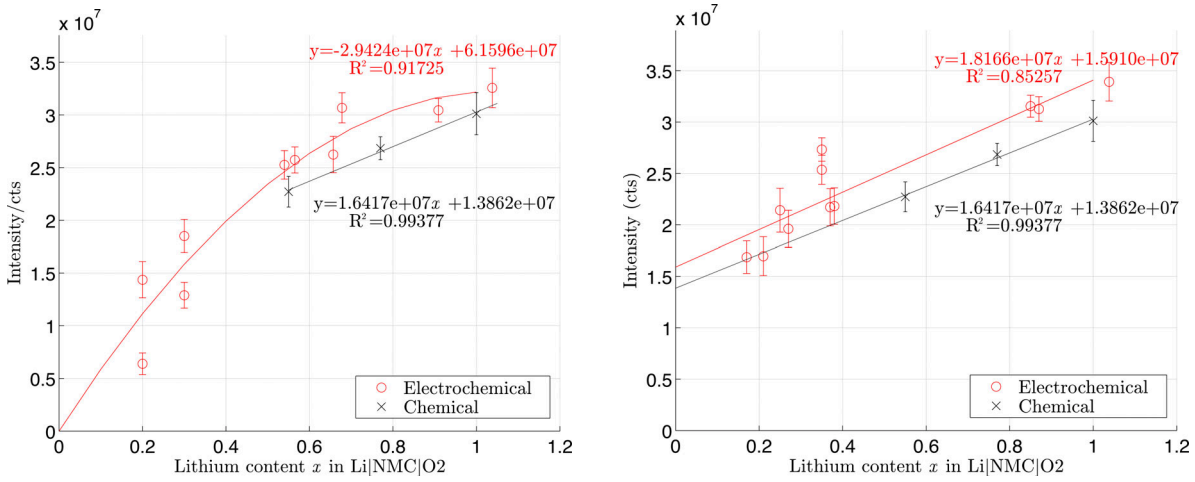

Figure 4.3 Calibration curve of lithium in Li_xNMCO_2 a) C/10 charge rate and b) C/50 charge rate

Figure 4.3 a shows the lithium intensities in TOF-SIMS for cathodes cycled at C/10. The intensities show a highly polynomial behavior that can be extrapolated towards the origin. This polynomial behaviour is confirmed by theoretical TRIM simulations of the lithium sputtering yield in NMC compounds (Supplementary Figure **4.3**). The experimental curves show rapidly decreasing intensities at low lithium content (x<0.5). Wu et al. showed that the lithium diffusion coefficient increases with increasing SOC - that is Li diffusion is facilitated in compounds with low lithium stoichiometry [4.31]. This higher diffusion coefficient at low Li content could explain the observed sharp decrease in intensity below x=0.5. XRD measurements on the cathodes with low lithium content (x≈ 0.2 and 0.3) showed distinct phase heterogeneities such that indexing the Li content was impossible, explaining the variability in the recorded intensities in the graph. Many studies have noticed state-of-charge (SOC) heterogeneities, which lead to Li-rich and Li-poor phases in the secondary particles. These heterogeneities are usually enhanced by high cycling rates, and can lead to capacity fade and local overcharge or discharge [4.30]. In an attempt to reduce the phase inhomogeneity, new coin-cells were prepared and cycled at very low rates, the lower current favouring more stability in lithium intercalation in the compound, as confirmed by XRD (see Supplementary Figure **4.6**).

Figure 4.3 b reports the results of the NMC cathodes cycled at C/50. The electrochemi-

cal calibration curve at C/50 exhibits an extrapolated non-null y-intercept, ΔY, as does the chemical curve in which we expect null lithium intensity if the cathode was completely delithiated. Especially at low lithium content, a C/50 charging rate resulted in overestimation of the lithium content in the material. Local segregation of lithium and deactivated particles may explain the added lithium signal. Cracking of primary particles as a result of cycling can further emphasize SOC heterogeneities [4.30] as well as relative position of the secondary particles within the cathode itself, where gradients of lithium ion concentrations were observed along the thickness of the NMC cathodes and in function of the particle size [4.32]. XRD studies have also shown that the crystalline NMC matrix suffers from anisotropic volume change during both chemical and electrochemical delithiation, leading to stress within the matrix. The primary particles may then be subject to disconnection from the NMC matrix, leading to the observed bulk inhomogeneities since the primary particles no longer participate in the delithiation process [4.30, 4.33]. Isolated particles from the electrochemical network retain more lithium compared to the connected matrix [4.32], and might explain the added ΔY in the calibration curve. We think the residual lithium seen in the TOF-SIMS intensities is not a consequence of sample preparation or handling, but rather a quantity of lithium ions that is not possible to extract from the material – whether chemically or electrochemically. Finally, another avenue to explain ΔY is the formation of a surface reconstruction layer in the secondary particles, creating a gradient layer on the surface of the particles, driven by the high reactivity of oxygen close to the particle surface [4.30]. During both delithiation processes, Ni becomes somewhat oxidized and Li depleted at the surface. Tian et al (2018) found that chemical delithiation with strong oxidizing agents lead to different surface chemistry than electrochemical processes, an effect that was observed for the highest SOC (low lithium content) with NO_2BF_4. This disparity could explain the variability between the extrapolated two curves in ΔY. This phenomenon was also observed at the nanoscale in LiNMO (where N=Ni, M=Mn) batteries and has proven to lead to increase of transition metal concentration as well as shortage of lithium at the surface of the particles [4.33]. By using very low changing rates, the SOC inhomogeneities have a larger time to set, making it more difficult to extract Li ions during discharge.

4.3.3 Assessment of edge effects in ion distributions and other phenomena

Figure 4.4 shows SIMS ions distribution of the active elements in the NMC cathodes, as well as before and after FIB secondary electron (SE) images of the analysis regions for a) a pristine sample (uncycled) and b) an electrode with SOC=100%. The image before and after SIMS analysis allows us to fully understand the effect of the analysis on the samples, as well as the effect of cycling. Before the analysis, the FIB SE image reveals NMC secondary grains of spheroidal shape, containing primary grains with clear contrast variations. The SE images after analysis for both samples show loss of contrast in the primary grains, associated with Ga ion implantation in the material which causes amorphization [4.25], as well as modification of the grain surface. Furthermore, sputtering is a destructive technique which removes material layer by layer from the material surface. On the cycled sample, it is evident that cycling changed the morphology of the NMC grains, creating cracks in the particles at grain boundaries. These cracks, which allow a change in topography of the samples, are emphasized during the cycling and allow enhanced sputtering since these positions have a favorable angle of incidence with the primary ion beam. These cracks lead to higher intensity of ion distributions and can be identified as edge effects. Edge effects are also expected at the periphery of particles, which are also observed in samples a and b. Differences in milling rates between adjacent grains of different crystallographic orientation [4.29] can also emphasize creation of edge effects, since grains in a channeling direction will have lower milling rates because the collision cascades occur deeper in the material [4.34], and hence sputtering is reduced.

Therefore, to determine the true concentration of lithium in the samples, edge effects must be distinguished from real signal variations from local compositional changes, and to do so, another source of information is needed to properly interpret the data. According to the FIB SE images in **Figure 4.4**, it is possible to link regions with altered topography that present high brightness on the SE image and with the occurrence of edge effects in ion distributions. Since high brightness indicates generally high topography, these regions can be disregarded for determining the Li intensity of the NMC grain. Confocal microscopy can also be used for surface analysis (after sputtering) to view the topography. Work is currently underway, but

not shown here, to link roughness from confocal measurements to intensities of the elements in the ion distributions.

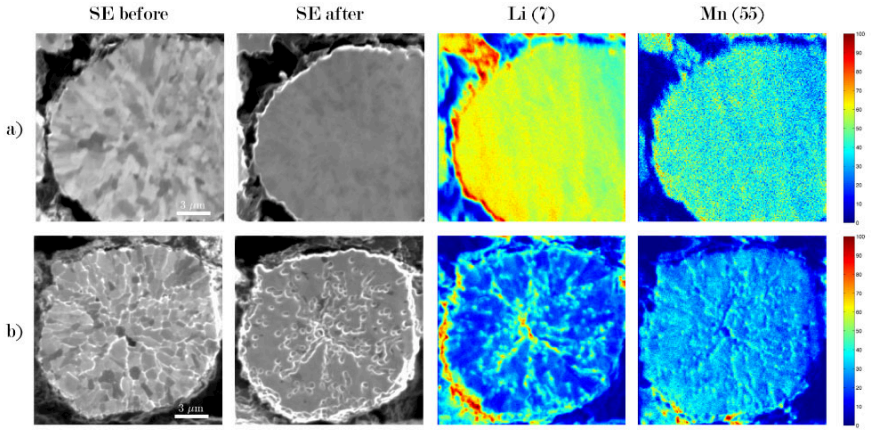

Figure 4.4 FIB SE images before and after analysis and ion distributions of Li, Mn of pristine (a) and cycled (b) cathode. The ions maps represent the cumulative data over 100 frames of analysis and normalized according to the maximum intensity in the species for each sample.

Not all regions with high intensities are related to edge effects. It is possible to observe grains with high lithium counts associated with a channeling crystallographic direction (low brightness) on the FIB SE image as shown in **Figure 4.5 a**. In the channeling direction, less information is recorded by the TOF-SIMS detector since less sputtering occurs by the primary ion beam. Therefore, the intensities of all the elements should be reduced compared to a non-channeling direction. These crystallographic effects in primary grains are seen, for example, in **Figure 4.5 b**. In the particular case of the grain in **Figure 4.5 a**, Mn, Ni and Co follow the expected crystallographic trends. Lithium, however, shows an increased number of counts. Channeling grains with this high amount of lithium were not found in pristine samples. Therefore, one must conclude that this observation is a result of the electrochemical activity that the cathodes have undergone. It is known that lithium ions may remain trapped at grain boundaries or at triple join points as a result of charge-discharge cycles and contribute to the degradation mechanisms [4.19]. These trapped ions were identified by Sui

al (2015) as “lithium hotspots”, which indicate an incomplete electrochemical reaction inside the NMC grains. In their paper, the presence of these hotspots was also linked with battery degradation and capacity fade. Results in this study show, however, that lithium hotspots are not found at the grain boundaries, but rather in the primary grains. Grain boundaries in **Figure 4.5** clearly show enhanced intensities, but according to our previous analysis regarding FIB SE imaging of the NMC grains and the analysis of edge effects, these increases in the analytical signal should be attributed to the topography obtained by sputtering at non-normal incidence.

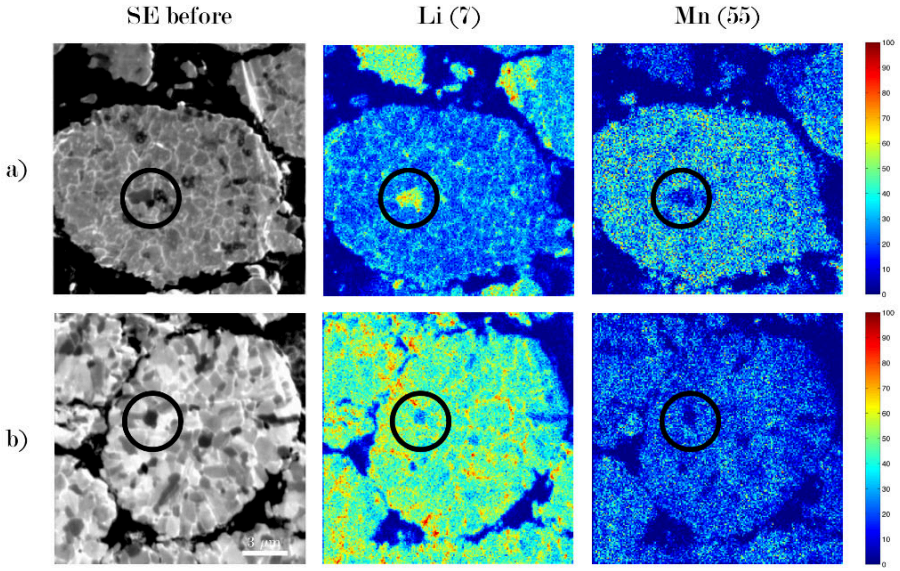

Figure 4.5 FIB SE image before TOF-SIMS analysis and ion distributions (Li and Mn) showing identification of a) crystallographic effect and b) electrochemical effect related to the apparent intensity of lithium in channeling grain versus the background matrix (of non-channeling orientation). Ion map distributions were normalized to the maximum in each species for each sample. In both cases, manganese follows the expected trend of a channeling direction.

4.4 Conclusion

In this work, a TOF-SIMS detector mounted on a FIB-SEM platform was used to detect lithium in standard NMC cathodes with different state-of-charge, and this technique is proposed as a solution to the detection limitation of EDS for lithium. High-resolution elemental distribution of active elements in NMC cathodes were obtained, allowing the identification of various phenomena resulting from sputtering. Both crystallographic and chemical effects were observed in primary grains in the ion maps. It was shown that edge effects can be correlated with high sample topography in SE images, and these regions on NMC grains were disregarded to avoid false analysis. High intensities of lithium at grain boundaries are the result of edge effects and artifacts in the analysis. Further investigations will be made to automate the identification of edge effects with correlative confocal microscopy. The quantification of lithium content in NMC cathodes with different state of charge was achieved using a calibration curve. This approach is a solution to the existing SIMS quantification method that did not provide meaningful results with the battery materials. At C/10 a polynomial relationship that corresponds to TRIM theoretical simulation of lithium extraction from a NMC matrix was found. An indirect linear relationship was found between lithium content in the NMC compounds (x) and measured TOF-SIMS intensities at C/50, which we believe is attributed to SOC heterogeneities within the secondary particles, as well as reconstruction of a surface layer and lithium segregation. Due to the matrix effects that are inherent to the technique, determining the Li concentration with the calibration curve applies only to our standard NMC. A specific experimental calibration curve is needed for each material for which the Li concentration is required because each material will exhibit different emission response to the primary ion-beam sputtering, once again as a result of matrix effects. Work is currently ongoing to quantify the Li content in lithium iron phosphate (LFP) cathodes, but since the primary grains are of the order 100 to 200 nm, there is an enhanced edge effect compared to NMC. Consequently, more work is required to optimize the technique for the analysis of LFP particles.

4.5 Experimental Methods

Cathode sample preparation

A slurry was prepared by mixing Li[NiCoMn]O_2 powder, conductive carbon and PVdF binder with a net ratio of 93:4:3, and using NMP solvent. The slurry was coated on the aluminum foil and dried at 110°C under vacuum to remove the solvent and residual moisture. The dry electrode had the loading of 10.5 mg cm^{-2} and the density after calendaring was controlled to 2.9 g cm^{-3}.

Cell assembly and SOC control

The cathode was assembled in a CR2032-type coin cell inside a He-filled glove box, using commercial lithium metal foil (200 μ m thick) and ceramic-coated porous polyethylene film (W-Scope) as anode and separator, respectively. The electrolyte was 1M $LiPF_6$ in EC:EMC (3:7). The coin cell was first charged to 4.5 V at 0.1C and fully discharged to 3.0 V. Then the cells were charged at the desired C-rate (C/10 or C/50) until the calculated capacity to control the degree of lithiation was obtained. We assumed that x=1 at the fully discharged state and the theoretical capacity is 277.6 mAh g^{-1} where x=0. The galvanostatic charge and discharge was performed using a cycler (VMP3, BIOLOGICS). For the analysis of cathode electrodes, the coin cells were carefully dismantled in the glove box and the electrodes were washed with DMC and dried before transferring to the instrument used in the chemical and surface analysis.

Chemical delithiation of NMC powders

NMC powder (5 g) was dispersed in a solution containing acetonitrile (100 ml), and the proper quantities of Br_2 as oxidizing agent (dibromide, Br_2, $\geq$ 99.99% trace metals basis, Sigma-Aldrich) were added to the solution and stirred magnetically overnight. The final powders were precipitated and rinsed with acetonitrile and ethanol. Before SIMS analysis, the NMC were dried in an oven for 24 hrs.

TOF-SIMS measurements

Cross-sections of the cycled cathodes were prepared using the Ar ion milling system IM4000 PLUS by Hitachi High Technologies to produce a flat surface for the TOF-SIMS analysis and to reduce the occurrence of edge effect at the source. Measurements with a confocal microscope [VK-X series, Keyence Laboratories] revealed a roughness of less than 150 nm at the surface of the milled particles. FIB milling in the FIB-SEM microscope [LYRA3 GT, TESCAN] was also investigated to prepare samples with lower roughness of the particles, but was discarded due to gallium poisoning that limited surfaces for analysis of the prepared trenches and added time/expense for preparation.

TOF-SIMS results were achieved using TESCAN's Lyra3 GT FIB-SEM microscope. The Cobra Ga+ ion column has 2.5 nm resolution at 30 keV, and the SEM is a field emission with a resolution of 2 nm at 5 keV. The microscope is equipped with a TOF-SIMS detector mounted on one of the upper ports of the SEM chamber. This TOF-SIMS analyzer is a result of the collaborative work of TESCAN and TOFWERK AG. The FIB column provides the primary ion source for the TOF-SIMS technique, where the bombardment of the Ga ions on the sample surface, and the resulting collision cascade will eject surface atoms. The ejected atoms, called secondary species, can be neutral, electrons, molecules and ions. The ionized particles (single elements or molecules) produced secondary ions (SI) that were collected in the mass analyzer by applying a potential difference. Upon entry, the SI will be accelerated at 5 kV and drift in the mass analyzer along a fixed distance, called drift length, until they reach the detector that will sort them according to their arrival time. In order for sufficient data to be collected to construct ion maps of the observed region, in this case a raster of 768x768 pixels over a region of 15x15 m is conducted with the FIB with 20 nm resolution in both direction (x and y). Data was collected over 100 frames (consisting of complete rasters over the 15x15 analysis area). TOF-SIMS provides both ion distributions over the whole analysis area, as well as mass spectra at each location, provided the integration over 100 frames of analysis.

The cathode cross-sections were mounted on a stud and inserted in the FIB-SEM microscope chamber with the cross-section perpendicular to the electron beam. The TOF-SIMS analysis

was performed with the sample tilted at a 55° using the TESCAN motorized stage so that the cross-section is perpendicular to the FIB column (which is positioned at a 55° angle relative to the electron column). Since sputtering is a function of the angle of incidence between the incident beam and the sample surface, this step produced good results and facilitated data interpretation. Ga primary ion energy of 30 keV and beam current of 500 pA were used to collect data. A negative potential difference was applied in the TOF-SIMS device in order to collect positive ions, which were the positive-charged elements of interest. The mass-to-charge (m/z) ratios were calibrated using $^{7}Li^{+}$, $^{55}Mn^{+}$ and $^{69}Ga^{+}$.

In order to compute the lithium intensities, multiple regions of interest (ROI) in the analysis regions were defined using the TOFWERK program and the mass spectra relative to those ROI computed. The ROIs were chosen to avoid the porosity in the areas between NMC particle grains, particles located in secondary planes, as well as edges effects as explained in the text. A simple integration of the desired peak was useful to determine the lithium peak intensity.

XRD measurements

X-ray diffraction (XRD) analyses were performed on the dried cathodes in order to confirm the lithium content in each of the cycled electrodes and the pristine sample. The XRD spectra are collected on a SmartLab diffractometer (Rigaku) with Co K radiation. The Rietveld refinement is conducted by using PDXL2 software (Rigaku). The spectra are refined in the $R\bar{3}m$ space group. Li and Ni cation mixing is kept at 0.035 (PDF 01-075-3920). Only the lithium content on the Li site is refined. The total Li content in the structure is the sum of the Li on Li site and Li on Ni site.

Acknowledgements

The authors would like to thank Daniel Clément, Vincent Gariépy and Catherine Gagnon for their technical assistance. This work was financed by Hydro-Québec's Research Institute, Center of Excellence in Transportation Electrification and Energy Storage,

Author contributions

S.B., R.G. K.Z. designed the experiment. S.B. proceeded to the sample preparation, measurement and analysis as well as wrote the manuscript. C.K. and A.P. provided the specimens. P.H., R.G. A.P. contributed to data interpretation. All authors reviewed the manuscript.

Additional information

The authors declare no competing financial interests.

Bibliography

[4.1] D. E. Newbury and D. B. Williams. The electron microscope: the materials characterization tool of the millennium. *Acta Materialia*, 48(1):323-346, 2000.

[4.2] S. Burgess, X. Li, and J. Holland. High spatial resolution energy dispersive X-ray spectrometry in the SEM and the detection of light elements including lithium. *Microscopy and Analysis*, 27:S8-S12, 2013.

[4.3] P. Hovington, V. Timoshevskii, S. Burgess, H. Demers, P. Statham, R. Gauvin, and K. Zaghib. Can we detect Li K X-ray in lithium compounds using energy dispersive spectroscopy?. *Scanning*, 38(6):571-578, 2016.

[4.4] J. H. Hubbell, P. N. Trehan, N. Singh, B. Chand, D. Mehta, M. L. Garg, R. R. Garg, S. Singh, and S. Puri. A Review, Bibliography, and Tabulation of K, L, and Higher Atomic Shell X-Ray Fluorescence Yields. *Journal of Physical and Chemical Reference Data*, 23(2):339-364, 1994.

[4.5] R.F. Egerton. *Electron Energy-Loss Spectroscopy in the Electron Microscope*. Language of Science. Springer,New York, 1996.

[4.6] S. Muto and K. Tatsumi. Detection of local chemical states of lithium and their spatial mapping by scanning transmission electron microscopy, electron energy-loss spectroscopy and hyperspectral image analysis. *Microscopy*, 66(1):39-49, Feb. 2017.

[4.7] CAMECA. *NanoSIMS 50L - Introduction to the instrumentation*. CAMECA, Product Brochure, 2017.

[4.8] ION-TOF. *TOF.SIMS5*. ION-TOF, Product Brochure.

[4.9] Physical Electronics. *PHI NanoTOFII - Time-of-Flight Secondary Ion Mass Spectrometer with Parallel Imaging MS/MS for Confident Molecular Identification*. Physical Electronics, Product Brochure.

[4.10] T. Sakamoto, M. Koizumi, J. Kawasaki, and J. Yamaguchi. Development of a high lateral resolution TOF-SIMS apparatus for single particle analysis. *Applied Surface Science*, 255(4):1617-1620, 2008. Proceedings of the Sixteenth International Conference on Secondary Ion Mass Spectrometry, SIMS XVI.

[4.11] F. A. Stevie, L. Sedlacek, P. Babor, J. Jiruse, E. Principe, and K. Klosova. FIB-SIMS quantification using TOF-SIMS with Ar and Xe plasma sources. *Surface and Interface Analysis*, 46(S1):285-287, 2014.

[4.12] L. Alberts, D.and von Werra, U. Ostlund, F.and Rohner, M. Hohl, J. Michler, and J. Whitby. Design and performance of two orthogonal extraction time-of-flight secondary ion mass spectrometers for focused ion beam instruments. *Instrumentation Science& Technology*, 42(4):432-445 2014.

[4.13] J. Whitby, F. Ostlund, P. Horvath, M. Gabureac, J. Riesterer, I. Utke, M. Hohl, L. Sedlacek, J. Jiruse, V. Friedli, M. Bechelany, and J. Michler. High spatial resolution time-of-flight secondary ion mass spectrometry for the masses: A novel orthogonal ToF FIB- SIMS instrument with In Situ AFM. *Advances in Materials Sciences and Engineering*, vol. 2012, Article ID 180437, 13 pages, 2012.

[4.14] M. Ohnishi, O. Matsuoka, H. Nogi, and T. Sakamoto. Observation of a $LiCoO_2$ cathode material of a li-ion battery by high spatial resolution TOF-SIMS. *e-Journal of Surface Science and Nanotechnology*, 10:207-209, 2012.

[4.15] A. Fedorkova, R. Orinakova, A. Orinak, I. Talian, A. Heile, H.-D. Wiemhofer, D. Kaniansky, and H. F. Arlinghaus. PPy doped PEG conducting polymer films synthesized on LiFePO4 particles. *Journal of Power Sources*, 195(12):3907-3912, 2010.

[4.16] A. Fedorkova, R. Orinakova, A. Orinak, A. Heile, H.-D. Wiemhofer, and H. F. Arlinghaus. Electrochemical and TOF-SIMS investigations of PPy/PEG-modified LiFePO4 composite electrodes for Li-ion batteries. *Solid State Sciences*, 13(5):824-830, 2011.

[4.17] J.-T. Li, J. Swiatowska, V. Maurice, A. Seyeux, L. Huang, S.-G. Sun, and P. Marcus. XPS and ToF-SIMS study of Sn-Co alloy thin films as anode for lithium ion battery. *Journal of Power Sources*, 195(24):8251-8257, 2010.

[4.18] J.-T. Li, J. Swiatowska, V. Maurice, A. Seyeux, L. Huang, S.-G. Sun, and P. Marcus. XPS and ToF-SIMS Study of Electrode Processes on Sn-Ni Alloy Anodes for Li-Ion Batteries. *The Journal of Physical Chemistry C*, 115(14):7012-7018, 2011.

[4.19] T. Sui, B. Song, J. Dluhos, L. Lu, and A. M. Korsunsky. Nanoscale chemical mapping of Li-ion battery cathode material by FIB-SEM and TOF-SIMS multi-modal microscopy. *Nano Energy*, 17:254-260, 2015.

[4.20] P. Sigmund. Theory of sputtering. I. sputtering yield of amorphous and polycrystalline targets. *Physical Review*, 184(2):383-416, 1969.

[4.21] K. B. Cheney and E. T. Pitkin. Sputtering at acute incidence. *Journal of Applied Physics*, 36(11):3542-3544, 1965.

[4.22] B.G. Yacobi, L.L. Kazmerski, and D.B. Holt. *Microanalysis of Solids*. Springer US, 2013.

[4.23] F. A. Stevie. *Secondary ion mass spectrometry : applications for depth profiling and surface characterization*. New York: Momentum Press, 2016.

[4.24] P. Williams. Secondary ion mass spectrometry. *Annual Review of Materials Science*, 15(1):517-548, 1985.

[4.25] L. A. Giannuzzi and F. A. Stevie. *Introduction to focused ion beams : instrumentation, theory, techniques, and practice*. New York: Springer, 2005.

[4.26] J. F. Ziegler, J.P. Biersack, and U. Littmark. *The stopping range of ions in solids, Vol. 1*, Pergamon Press, New York, 1985.

[4.27] J.F. Ziegler, J.P. Biersack, and M.D. Ziegler. SRIM, the Stopping and Range of Ions in Matter. SRIM Company, 2008.

[4.28] B. G. Svensson, M. K. Linnarsson, B. Mohadjeri, M. Petravic, and J. S. Williams. SIMS and depth profiling of semiconductor structures. *Nuclear Instruments and Methods in Physics Research Section B: Beam Interactions with Materials and Atoms*, 85(1):363-369, 1994.

[4.29] B. W. Kempshall, S. M. Schwarz, B. I. Prenitzer, L. A. Giannuzzi, R. B. Irwin, and F. A. Stevie. Ion channeling effects on the focused ion beam milling of Cu. *Journal of Vacuum Science and Technology B: Microelectronics and Nanometer Structures Processing, Measurement, and Phenomena*, 19(3):749-754, 2001.

[4.30] C. Tian, Y. Xu, D. Nordlund, F. Lin, J. Liu, Z. Sun, Y. Liu, and M. Doeff. Charge heterogeneity and surface chemistry in polycrystalline cathode materials. *Joule*, 2(3):464-477, 2018.

[4.31] S.-L. Wu, W. Zhang, X. Song, A. K. Shukla, G. Liu, V. Battaglia, and V. Srinivasan. High Rate Capability of $Li(Ni_{1/3}Mn_{1/3}Co_{1/3})O_2$ Electrode for Li-Ion Batteries. Journal of The Electrochemical Society, 159(4):A438-A444, 2012.

[4.32] L. Wu, X. Xiao, Y. Wen, and J. Zhang. Three-dimensional finite element study on stress generation in synchrotron X-ray tomography reconstructed nickel-manganese-cobalt based half cell. Journal of Power Sources, 336:8-18, 2016.

[4.33] A. Devaraj, M. Gu, R. Colby, P. Yan, C. M. Wang, J. M. Zheng, J. Xiao, A. Genc, J. G. Zhang, I. Belharouak, D. Wang, K. Amine, and S. Thevuthasan. Visualizing nanoscale 3D compositional fluctuation of lithium in advanced lithium-ion battery cathodes. *Nature Communications*, 6:8014, 2015.

[4.34] B. Schmidt and K. Wetzig. *Ion Beams in Materials Processing and Analysis*. Springer Vienna, 2012.

[4.35] L. Li, D. S. McPhail, N. Yakovlev, and H. Seng. Strategies for improving the sensitivity of FIB-SIMS. *Surface and Interface Analysis*, 43(1-2):495-497, 2011.

[4.36] D. S. McPhail, L. Li, Richard J. Chater, N. Yakovlev, and H. Seng. From FIB-SIMS to SIMS-FIB. The prospects for a 10 nm lateral resolution SIMS instrument with full FIB functionality. *Surface and Interface Analysis*, 43(1-2):479–483, 2011.

NANOSCALE LITHIUM QUANTIFICATION IN $Li_xNi_yCo_wMn_zO_2$ AS CATHODE FOR RECHARGEABLE BATTERIES

Stéphanie Bessette[1,2], Andrea Paolella[1], Chisu Kim[1], Wen Zhu[1], Pierre Hovington[3], Raynald Gauvin[2] and Karim Zaghib[1,*]

[1] *Hydro-Québec's Research Institute, Center of Excellence in Transportation Electrification and Energy Storage, Varennes, J3X 1S1, Canada*

[2] *McGill University, Department of Mining and Materials Engineering, Montréal, H3A 0C5, Canada*

[3] *Consulting Hovington, Boucherville, Québec, Canada*

*E-mail: Zaghib.Karim@ireq.ca

Supplementary Information

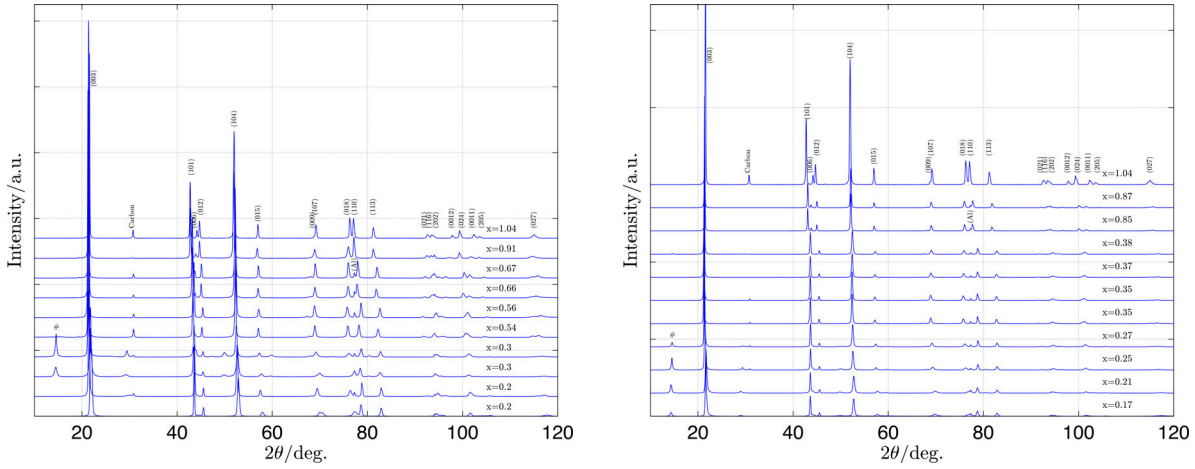

Figure 4.6 XRD spectra of electrochemically delithiated NMC cathodes.The (hkl)s of main phase NMC peaks are labelled for a) C/10 and b) C/50 cycling rates. The (018) and (110) peaks are close in the fully lithiated NMC, whereas they are further apart in the partially lithiated structure. In addition, (006) of fully lithiated NMC is seen at $\sim 44°$, but it is not seen in partially lithiated NMC. Carbon from the binder is seen in some of the spectra as well as aluminum (220) from the electrode collector. The labelled peak is impurity in the material, seen only at low lithium content.

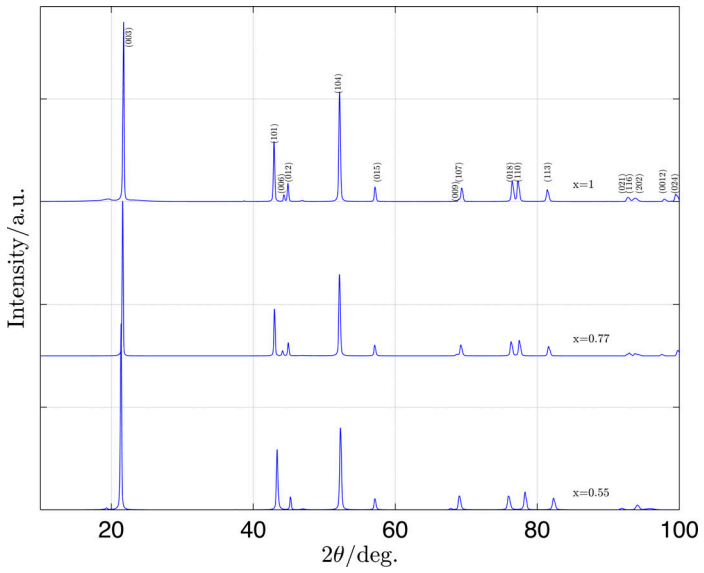

Figure 4.7 XRD spectra of chemically delithiated NMC powder. The (hkl)s of main phase NMC peaks are labelled in the graph. Once again, the (018) and (110) peaks are close in the fully lithiated NMC whereas they are further apart in the partially lithiated structure. In addition, (006) of fully lithiated NMC is at $\sim 44°$, but it is not seen in partially lithiated NMC.

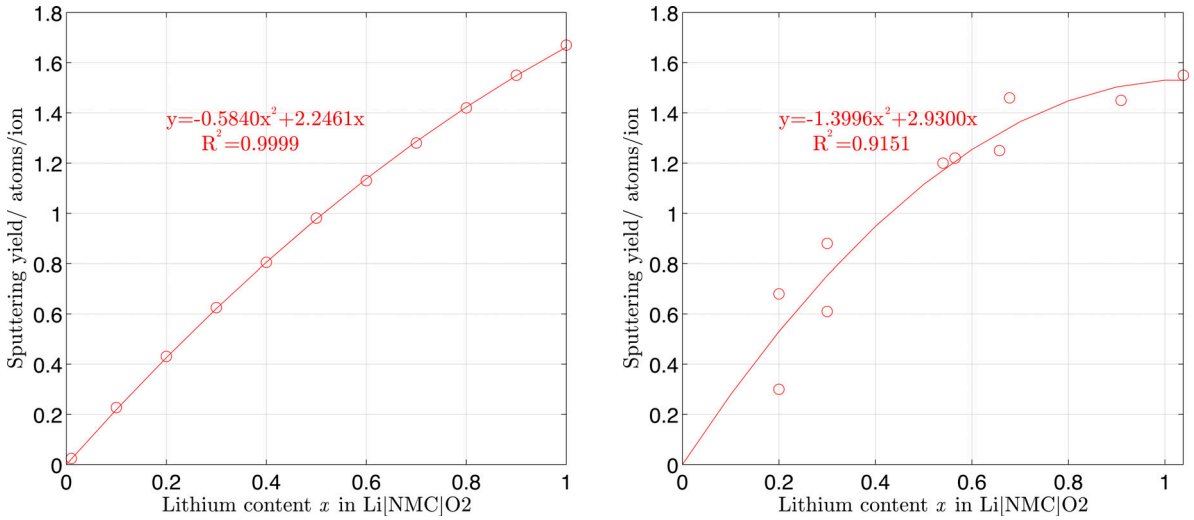

Figure 4.8 a)TRIM simulations of elemental sputtering yield of lithium atoms in $Li_x[NMC]O_2$ compounds with varying lithium stoichiometry. Simulations were done using surface sputtering mode with 100 000 Ga ions with incident energy of 30 keV to reproduce experimental conditions. b) Conversion of experimental intensities (results shown in **Figure 4.3 a**) into sputter yields for comparison with theoretical yields. Calculations were made starting from the basic SIMS equation for secondary species signal $I(X^+) = Y_X \cdot V \cdot \rho_X$ [4.35, 4.36] where $I(X^+)$ is the secondary ion specie of interest, Y_X is the useful yield, V the analytical volume and the concentration of the desired specie in matrix. The useful yield is by definition the product of the ionization efficiency α of analyte and the transmission efficiency (T) of said ions within the SIMS apparatus. A value of 10^{-6} for the useful yield Y_X was used for calculations, which is typical for FIB-SIMS analysis [4.36] . Results show a similar polynomial behavior between the experimental and the simulated sputter yield for lithium ions by gallium primary ions.

CHAPTER 5 SUMMARY

The main objective of this research was to develop characterization technique in a FIB-SEM platform that could permit both lithium detection and quantification for battery materials. This work was conducted on lithium nickel manganese cobalt oxide cathodes as a proof of concept of the experimental technique developed in response to the complex nature of battery materials that couldn't comply with standard SIMS quantification technique with relative sensitivity factors (RSF). This insertion material allowed different stoichiometry of lithium in a complex compound. The present section provides a summary of the work accomplished.

- A portable TOF-SIMS (TOFWERKS) detector mounted on a TESCAN FIB-SEM platform allowed both detection and quantification of lithium. This preferred technique was chosen to overcome EDS's detection limitation regarding lithium atoms in compounds and as a solution to the overlap of Li ionization edge with transition metal $M_{2,3}$ edges in EELS.

- Matrix effect resulting in an increase in sputtering of light lithium atom in NMC compound was proven both experimentally and using TRIM simulations.

- Due to the complex nature of NMC compared to semiconductor materials that are typically studied in SIMS, the suggested quantification method using relative sensitivity factors (RSF) was found obsolete. An experimental calibration curve depicting lithium ion intensity as a function of Li stoichiometry in NMC was found to give good correlation and repeatability.

- The experimental calibration curve holds for the analysis condition used. Adjustments to the calibration curve are needed if primary ion current, analysis area, ion energy, etc... are modified since they will imply a change in the sputtering of the sample's atom. Likewise, for quantification of lithium ions in another compound like LFP, the experimental calibration curve has to be constructed from scratch.

- Optimal sample preparation in minimized roughness of the cathode cross-sections, which in turn resulted in a decrease of edge effect. However, sample artefacts such

as cracks resulting from cycling and differences in crystallographic orientation of adjacent grains can still trigger edge effects. As a result, it was found that comparing FIB SE images with ion distributions can help identify edge effects from crystallographic and chemical phenomena (for example lithium hotspots). Careful selection of regions of interest (ROI) for quantitative analysis is therefore indicated to obtain true lithium concentration in the material.

REFERENCES

[1] United Nations Framework Convention on Climate Change. Paris Agreement - Status of Ratification. Available at https://unfccc.int/process/the-paris-agreement/status-of-ratification, 2018.

[2] Governement of Canada. Canada's INDC submission to the UNFCCC. Available at http://www4.unfccc.int/submissions/INDC/Published%20Documents/Canada/1/INDC%20-%20Canada%20-%20English.pdf, 2015.

[3] Hydro-Québec. Sustainability report 2016. Available at http://www.hydroquebec.com/data/developpement-durable/pdf/sustainability-report-2016.pdf?v=20170529, 2017.

[4] Hydro-Québec. Le Québec, un chef de file mondial des matériaux de batteries. Available at http://nouvelles.hydroquebec.com/fr/communiques-de-presse/1317/, March 23, 2018. [Press Release].

[5] M. Primeau. Le Québec, bientôt producteur de batteries? Available at http://plus.lapresse.ca/screens/f0cf3b38-8892-42f9-bdc7-827d1d3bbdce__7C___0.html, April 9, 2018.

[6] F. A. Stevie. *Secondary ion mass spectrometry : applications for depth profiling and surface characterization*. New York: Momentum Press, 2016.

[7] A.J. Bard and L.R. Faulkner. *Electrochemical Methods: Fundamentals and Applications*. New York: Wiley, 2001.

[8] M. Stanley Whittingham. Lithium batteries and cathode materials. *Chemical Reviews*, 104(10):4271–4302, 2004. PMID: 15669156.

[9] C. Julien, A. Mauger, A. Vijh, and K. M Zaghib. *Lithium batteries : science and technology*. Springer International Publishing, 2016.

[10] M. Winter, J. Besenhard, M.E. Spahr, and P. Novak. Insertion electrode materials for rechargeable lithium batteries. *Advanced materials*, 10:725–725, 1998.

[11] P. Hovington, M. Lagacé, A. Guerfi, P. Bouchard, A. Mauger, C. M. Julien, M. Armand, and K. Zaghib. New lithium metal polymer solid state battery for an ultrahigh energy: nano C-LiFePO4 versus nano Li1.2V3O8. *Nano Letters*, 15(4):2671–2678, 2015. PMID: 25714564.

[12] J. Zhang, W. Xu, and W. A. Henderson. Li metal anodes and rechargeable lithium metal batteries. springer series in materials science.

[13] C. Brissot, M. Rosso, J.-N. Chazalviel, and S. Lascaud. Dendritic growth mechanisms in lithium/polymer cells. *Journal of Power Sources*, 81-82:925 – 929, 1999.

[14] F. Orsini, A. du Pasquier, B. Beaudouin, J.M. J.M. Tarascon, M. Trentin, N. Langenhuizen, E. de Beer, and Current density SEM Dendrite P. Notten", keywords = "Lithium electrode. In situ SEM study of the interfaces in plastic lithium cells. *Journal of Power Sources*, 81-82:918 – 921, 1999.

[15] M. Dollé, L. Sannier, B. Beaudoin, M. Trentin, and J.M. Tarascon. Live scanning electron microscope observations of dendritic growth in lithium/polymer cells. *Electrochemical and Solid-State Letters*, 5(12):A286–A289, 2002.

[16] C. Monroe and J. Newman. Dendrite growth in lithium/polymer systems: A propagation model for liquid electrolytes under galvanostatic conditions. *Journal of The Electrochemical Society*, 150(10):A1377–A1384, 2003.

[17] M. Rosso, C. Brissot, A. Teyssot, M. Dollé, J.M. Sannier, L.and Tarascon, R. Bouchet, and S. Lascaud. Dendrite short-circuit and fuse effect on Li/polymer/Li cells. 51:5334–5340, 07 2006.

[18] K. Nishikawa, T. Mori, T. Nishida, Y. Fukunaka, M. Rosso, and T. Homma. In situ observation of dendrite growth of electrodeposited li metal. *Journal of The Electrochemical Society*, 157(11):A1212–A1217, 2010.

[19] J. Steiger, D. Kramer, and R. Mönig. Mechanisms of dendritic growth investigated by in situ light microscopy during electrodeposition and dissolution of lithium. *Journal of Power Sources*, 261:112 – 119, 2014.

[20] A. Kushima, K.P. So, C. Su, P. Bai, N. Kuriyama, T. Maebashi, Y. Fujiwara, M.Z. Bazant, and J. Li. Liquid cell transmission electron microscopy observation of lithium metal growth and dissolution: Root growth, dead lithium and lithium flotsams. *Nano Energy*, 32:271 – 279, 2017.

[21] R. Jasinski. *High-energy batteries*. Plenum Press, 1967.

[22] M. B. Pinson and M.Z. Bazant. Theory of SEI formation in rechargeable batteries: capacity fade, accelerated aging and lifetime prediction. *Journal of The Electrochemical Society*, 160(2):A243–A250, 2013.

[23] V. Agubra and J. Fergus. Lithium ion battery anode aging mechanisms. 6:1310–1325, 03 2013.

[24] K. Xu. Nonaqueous liquid electrolytes for lithium-based rechargeable batteries. *Chemical Reviews*, 104(10):4303–4418, 2004. PMID: 15669157.

[25] J. Vetter, P. Novák, M.R. Wagner, C. Veit, K.-C. Möller, J.O. Besenhard, M. Winter, M. Wohlfahrt-Mehrens, C. Vogler, and A. Hammouche. Ageing mechanisms in lithium-ion batteries. *Journal of Power Sources*, 147(1):269 – 281, 2005.

[26] L. A. Giannuzzi and F. A. Stevie. *Introduction to focused ion beams : instrumentation, theory, techniques, and practice*. New York: Springer, 2005.

[27] J.I. Goldstein, D.E. Newbury, D. E, D.C. Joy, P. Echlin, C.E. Lyman, E. Lifshin, L. Sawyer, et al. *Scanning Electron Microscopy and X-ray Microanalysis: Third Edition*. Scanning Electron Microscopy and X-ray Microanalysis. Springer US, 2003.

[28] Orsay Physics. Scientific Overviews- What is UHV? [Online]. Accessed April 17th, 2018. Available at `http://www.orsayphysics.com/what-is-uhv`.

[29] TESCAN. *Lyra3 Microscope*. TESCAN ORSAY HOLDING, User manual, 2016.

[30] TESCAN. *LYRA3- Focused ion beam scanning electron microscope for high-performance in nanoengineering*. TESCAN ORSAY HOLDING, Product Brochure, 2016.

[31] C.A. Volkert and A.M. Minor. Focused Ion Beam Microscopy and Micromachining. *MRS Bulletin*, 32:389–399, 2007.

[32] H. Okamoto. Ga-Li (Gallium-Lithium). *Journal of Phase Equilibria and Diffusion*, 27:200–200, 03 2006.

[33] L. A. Mayer, J.and Giannuzzi, T. Kamino, and J. Michael. TEM Sample Preparation and FIB-Induced Damage. *MRS Bulletin*, 32(5).

[34] J.F. Ziegler, J.P. Biersack, and M.D. Ziegler. *SRIM, the Stopping and Range of Ions in Matter*. SRIM Company, 2008.

[35] H. Azza, N. Selhaoui, A. Iddaoudi, and L. Bouirden. Thermodynamic Reassessment of the Gallium–Lithium Phase Diagram. 38, 07 2017.

[36] J.D. Casey Jr., M. Phaneuf, C. Chandler, M. Megorden, K.E. Noll, R. Schuman, T.J. Gannon, A. Krechmer, D. Monforte, N. Antoniou, N. Bassom, J. Li, P. Peter Carleson, and C. Huynh. Copper device editing: Strategy for focused ion beam milling of copper. *Journal of Vacuum Science & Technology B: Microelectronics and Nanometer Structures Processing, Measurement, and Phenomena*, 20(6):2682–2685, 2002.

[37] N. Antoniou. Failure analysis of electronic material using cryogenic FIB-SEM. *Electronic Device Failure Analysis*, 15:12–19, 01 2013.

[38] T. Chou and M.E. Williams. Cryo-FIB minimizes Ga+ milling artifacts in Sn. *Microscopy and Microanalysis*, 20:328–329, 08 2014.

[39] M. F. Hayles, D. J. Stokes, D. Phifer, and K. C. Findlay. A technique for improved focused ion beam milling of cryo-prepared life science specimens. *Journal of Microscopy*, 226(3):263–269, 2007.

[40] B. Schmidt and K. Wetzig. *Ion Beams in Materials Processing and Analysis*. Springer Vienna, 2012.

[41] Y. Quéré. Dechanneling of fast particles by lattice defects. *Journal of Nuclear Materials*, 53:262 – 267, 1974.

[42] M.T. Robinson and O.S. Oen. The channeling of energetic atoms in crystal lattices. *Applied Physics Letters*, 2(2):30–32, 1963.

[43] B. W. Kempshall, S. M. Schwarz, B. I. Prenitzer, L. A. Giannuzzi, R. B. Irwin, and F. A. Stevie. Ion channeling effects on the focused ion beam milling of Cu. *Journal of Vacuum Science and Technology B: Microelectronics and Nanometer Structures Processing, Measurement, and Phenomena*, 19(3):749–754, 2001.

[44] U. Wendt and G. Nolze. FIB Milling and Canneling. *Imaging & Microscopy*, 53:262 – 267, 2008.

[45] D.B. Williams and C.B. Carter. *Transmission Electron Microscopy: A Textbook for Materials Science*. Number vol. 2 in Cambridge library collection. Springer, 2009.

[46] A.J. Tousimis and L. Marton. *Electron Probe Microanalysis*. Advances in Electronics and Electron Physics. Supplement. Elsevier Science, 2013.

[47] J.I. Goldstein, D.E. Newbury, P. Echlin, D.C. Joy, C. Fiori, and E. Lifshin. *Scanning electron microscopy and X-ray microanalysis: First Edition*. Plenum Press, 1981.

[48] S. Burgess, X. Li, and J. Holland. High spatial resolution energy dispersive X-ray spectrometry in the SEM and the detection of light elements including lithium. *Microscopy and Analysis*, 27:S8–S12, 2013.

[49] J.J. McCarthy, J.J. Friel, P. Camus, and D. Rohde. Impact of 40 years of technology advances on EDS system performance. *Microscopy and Microanalysis*, 14(S2):114–115, 2008.

[50] Oxford Instruments. *Silicon Drift Detectors Explained*. Oxford Instruments, 2012.

[51] D. B. Williams, J. I. Goldstein, and D. E. Newbury. *X-Ray Spectrometry in Electron Beam Instruments*. Springer, 01 1995.

[52] S. Burgess, J. Sagar, J. Holland, X. Li, and F. Bauer. Ultra-low kV EDS - a new approach to improved spatial resolution, surface sensitivity, and light element compositional imaging and analysis in the SEM. *Microscopy Today*, 25(2):20–29, 2017.

[53] R. Castaing. *UCRL-8381*. PhD thesis, University of Paris, 1958.

[54] G. Cliff and G. W. Lorimer. The quantitative analysis of thin specimens. *Journal of Microscopy*, 103(2):203–207.

[55] P. Horny, E. Lifshin, H. Campbell, and R. Gauvin. Development of a new quantitative x-ray microanalysis method for electron microscopy. *Microscopy and Microanalysis*, 16(6):821–830, 2010.

[56] R. Gauvin. What remains to be done to allow quantitative X-ray microanalysis performed with EDS to become a true characterization technique? *Microscopy and Microanalysis*, 18(5):915–940, 2012.

[57] J. H. Hubbell, P. N. Trehan, N. Singh, B. Chand, D. Mehta, M. L. Garg, R. R. Garg, S. Singh, and S. Puri. A Review, Bibliography, and Tabulation of K, L, and Higher Atomic Shell X-Ray Fluorescence Yields. *Journal of Physical and Chemical Reference Data*, 23(2):339–364, 1994.

[58] Central Facility for Advanced Microscopy and Microanalysis. Introduction to Energy Dispersice X-ray Spectrometry (EDS). University of California Riverside.

[59] P. Hovington, V. Timoshevskii, S. Burgess, P. Statham, H. Demers, R. Gauvin, and K. Zaghib. Towards Li Quantification at High Spatial Resolution Using EDS. *Microscopy and Microanalysis*, 22(S3):84–85, 2016.

[60] P. Hovington, V. Timoshevskii, S. Bessette, S. Burgess, P. Statham, H. Demers, R. Gauvin, and K. Zaghib. On the detection limits of Li K X-rays using windowless energy dispersive spectrometer (EDS). *Microscopy and Microanalysis*, 23(S1):2024–2025, 2017.

[61] T. Sui, B. Song, J. Dluhos, L. Lu, and A. M. Korsunsky. Nanoscale chemical mapping of Li-ion battery cathode material by FIB-SEM and TOF-SIMS multi-modal microscopy. *Nano Energy*, 17:254–260, 2015.

[62] P. Hovington, V. Timoshevskii, S. Burgess, H. Demers, P. Statham, R. Gauvin, and K. Zaghib. Can we detect Li K X-ray in lithium compounds using energy dispersive spectroscopy? *Scanning*, 38(6):571–578, 2016.

[63] R.F. Egerton. *Electron Energy-Loss Spectroscopy in the Electron Microscope*. Language of Science. Springer,New York, 1996.

[64] R.F. Egerton. Inelastic scattering of 80 keV electrons in amorphous carbon. *The Philosophical Magazine: A Journal of Theoretical Experimental and Applied Physics*, 31(1):199–215, 1975.

[65] R.F. Egerton. *Electron Energy-Loss Spectroscopy in the Electron Microscope, Third Edition*. Language of science. Springer, NewYork, 2011.

[66] R. Senga and K. Suenaga. Single-atom electron energy loss spectroscopy of light elements. *Nature communications*, 6:7943, 2015.

[67] F. Wang, J. Graetz, and Y. Zhu. In situ TEM-EELS for tracking lithium electrochemical reactions in single particles. *Microscopy and Microanalysis*, 18(S2):1324–1325, 2012.

[68] S. Muto and K. Tatsumi. Detection of local chemical states of lithium and their spatial mapping by scanning transmission electron microscopy, electron energy-loss spectroscopy and hyperspectral image analysis. *Microscopy*, 66(1):39–49, Feb. 2017.

[69] P. Sigmund. Theory of Sputtering. I. Sputtering Yield of Amorphous and Polycrystalline Targets. *Physical Review*, 184(2):383–416, 1969.

[70] R.G. Wilson, F.A. Stevie, and C.W. Magee. *Secondary Ion Mass Spectrometry*. Wiley, New York, 1989.

[71] F. A. Stevie, L. Sedlacek, P. Babor, J. Jiruse, E. Principe, and K. Klosova. FIB-SIMS quantification using TOF-SIMS with Ar and Xe plasma sources. *Surface and Interface Analysis*, 46(S1):285–287, 2014.

[72] F. Aubriet, C. Poleunis, and P. Bertrand. Investigation of the cluster ion formation process for inorganic compounds in static SIMS. 203:114–117, 01 2003.

[73] R. Van Ham, A. Adriaens, L. Van Vaeck, R. Gijbels, and F. Adams. Molecular information in static SIMS for the speciation of inorganic compounds. *Nuclear Instruments & Methods in Physics Research Section B-beam Interactions With Materials and Atoms*, 161:245–249, 03 2000.

[74] A. Hewavitharana, S. K. Tan, and P. N. Shaw. Strategies for the Detection and Elimination of Matrix Effects in Quantitative LC-MS Analysis. *LCGC North America*, 32:54–64, 01 2014.

[75] G.L. Fisher. TOF-SIMS data interpretation. Physical Electronics, [Online]. Accessed June 17th, 2016. Available at `http://mrllibrary.mrl.illinois.edu/rootfolder/5-Surface%20Science%20and%20Analysis%20Core/SIMS/TOF-SIMS/TOF-SIMS%20Data%20Interpretation.pdf`,.

[76] M. A. Makeev and A. L. Barabási. Effect of surface roughness on the secondary ion yield in ion sputtering. *Applied Physics Letters*, 73(15):2209–2211, 1998.

[77] S. J. Pachuta. Enhancing and automating TOF-SIMS data interpretation using principal component analysis. *Applied Surface Science*, 231-232:217 – 223, 2004. Proceedings of the Fourteenth International Conference on Secondary Ion Mass Spectrometry and Related Topics.

[78] CAMECA. *NanoSIMS 50L - Introduction to the instrumentation*. CAMECA, Product Brochure, 2017.

[79] J. Whitby, F. Östlund, P. Horvath, M. Gabureac, J. Riesterer, I. Utke, M. Hohl, L. Sedlacek, J. Jiruše, V. Friedli, M. Bechelany, and J. Michler. High spatial resolution time-of-flight secondary ion mass spectrometry for the masses: A novel orthogonal ToF FIB-SIMS instrument with In Situ AFM. *Advances in Materials Science and Engineering*, 2012(Article ID 180437):13 p., 2012.

[80] M.L. Yu. Chemical enhancement effects in SIMS analysis. *Nuclear Instruments and Methods in Physics Research Section B: Beam Interactions with Materials and Atoms*, 15(1):151 – 158, 1986.

[81] C.M. Mahoney. Cluster secondary ion mass spectrometry of polymers and related materials. *Mass spectrometry reviews*, 29:247–93, 01 2009.

[82] C.M. Mahoney. *Cluster Secondary Ion Mass Spectrometry: Principles and Applications*. New York: Wiley, 04 2013.

[83] ION-TOF. TOF-SIMS. [Online]. Accessed June 20th, 2018. Available at `https://www.iontof.com/tof-sims-secondary-ion-mass-spectrometry.html`.

[84] S. Chatterjee and M. Linford. Highlights from the 2016 Microscopy & Microanalysis Meeting in Columbus, OH. A New MS/MS Imaging ToF-SIMS Mass Spectrometer, a Very Low Cost AFM, and a Remote Plasma Cleaning System. *Vacuum Technology & Coating*, 09 2016.

[85] Physical Electronics. *PHI NanoTOFII - Time-of-Flight Secondary Ion Mass Spectrometer with Parallel Imaging MS/MS for Confident Molecular Identification.* Physical Electronics, Product Brochure.

[86] G. L. Fisher, J.S. Hammond, P.E. Larson, S.R. Bryan, and R.M.A. Heeren. Parallel imaging MS/MS TOF-SIMS instrument. *Journal of Vacuum Science & Technology B*, 34(3):03H126, 2016.

[87] D. Alberts, L. von Werra, F. Östlund, U. Rohner, M. Hohl, J. Michler, and J. Whitby. Design and performance of two orthogonal extraction time-of-flight secondary ion mass spectrometers for focused ion beam instruments. *Instrumentation Science & Technology*, 42(4):432–445, 2014.

[88] TOFWERK. Tofwerk modular design platform. [Online]. Accessed June 15th, 2018. Available at `https://www.tofwerk.com/products/custom/`.

[89] B. Hagenhoff. High Resolution Surface Analysis by TOF-SIMS. *Microchimica Acta*, 132(2):259–271, Apr 2000.

[90] T. Sakamoto, M. Koizumi, J. Kawasaki, and J. Yamaguchi. Development of a high lateral resolution TOF-SIMS apparatus for single particle analysis. *Applied Surface Science*, 255(4):1617–1620, 2008. Proceedings of the Sixteenth International Conference on Secondary Ion Mass Spectrometry, SIMS XVI.

[91] P.J. Linstrom and W.G. Mallard. NIST Chemistry WebBook, NIST Standard Reference Database Number 69, Gaithersburg MD, 20899.

[92] Liebl H. SIMS instrumentation and imaging techniques. *Scanning*, 3(2):79–89, 1980.

[93] ION-TOF. *TOF.SIMS5.* ION-TOF, Product Brochure.

[94] Mass Spectrometry Resource. Washington University in St. Louis - School of medicine. Available at `http://msr.dom.wustl.edu/reflectrons-ion-mirrors/`.

[95] M. Guilhaus. Principles and instrumentation in Time-of-Flight mass spectrometry: Physical and instrumental concepts. *Journal of Mass pectrometry*, 30(11):1519–1532, 1995.

[96] S. Patel and Mowat. I. Analytical techniques for detecting unwanted Fe particles in cathodes. [Online]. Accessed June 9th, 2016. Available at `www.eag.com/documents/ecsseattle12_spatel.pdf`.

[97] A. Fedorková, R. Oriňáková, A. Oriňák, I. Talian, A. Heile, H.-D. Wiemhöfer, D. Kaniansky, and H. F. Arlinghaus. PPy doped PEG conducting polymer films synthesized on LiFePO4 particles. *Journal of Power Sources*, 195(12):3907–3912, 2010.

[98] A. Fedorková, R. Oriňáková, A. Oriňák, A. Heile, H.-D. Wiemhöfer, and H. F. Arlinghaus. Electrochemical and TOF-SIMS investigations of PPy/PEG-modified LiFePO4 composite electrodes for Li-ion batteries. *Solid State Sciences*, 13(5):824–830, 2011.

[99] Evans Analytical Group. Battery technology. [Online]. Accessed May 11th, 2018. Available at `https://www.eag.com/wp-content/uploads/2017/02/battery-technology-M-014516.pdf`.

[100] J.-T. Li, J. Światowska, V. Maurice, A. Seyeux, L. Huang, S.-G. Sun, and P. Marcus. XPS and ToF-SIMS study of Sn-Co alloy thin films as anode for lithium ion battery. *Journal of Power Sources*, 195(24):8251–8257, 2010.

[101] J.-T. Li, J. Światowska, V. Maurice, A. Seyeux, L. Huang, S.-G. Sun, and P. Marcus. XPS and ToF-SIMS Study of Electrode Processes on Sn-Ni Alloy Anodes for Li-Ion Batteries. *The Journal of Physical Chemistry C*, 115(14):7012–7018, 2011.

[102] C.-K. ChiuHuang, C. Zhou, and H.-Y. Shadow Huang. In situ imaging of lithium-ion batteries via the secondary ion mass spectrometry. *Journal of Nanotechnology in Engineering and Medicine*, 5(2):021002–021002–5, 2014.

[103] A. Bordes, E. De Vito, C. Haon, C. Secouard, A. Montani, and P. Marcus. Investigation of Lithium Insertion Mechanisms of a Thin-Film Si Electrode by Coupling Time-of-Flight Secondary-Ion Mass Spectrometry, X-ray Photoelectron Spectroscopy, and Focused-Ion-Beam/SEM. *ACS Applied Materials & Interfaces*, 7(50):27853–27862, 2015.

[104] D. E. Newbury and D. B. Williams. The electron microscope: the materials characterization tool of the millennium. *Acta Materialia*, 48(1):323–346, 2000.

[105] M. Ohnishi, O. Matsuoka, H. Nogi, and T. Sakamoto. Observation of a $LiCoO_2$ Cathode Material of a Li-Ion Battery by High Spatial Resolution TOF-SIMS. *e-Journal of Surface Science and Nanotechnology*, 10:207–209, 2012.

[106] K. B. Cheney and E. T. Pitkin. Sputtering at acute incidence. *Journal of Applied Physics*, 36(11):3542–3544, 1965.

[107] B.G. Yacobi, L.L. Kazmerski, and D.B. Holt. *Microanalysis of Solids*. Springer US, 2013.

[108] P. Williams. Secondary ion mass spectrometry. *Annual Review of Materials Science*, 15(1):517–548, 1985.

[109] J. F. Ziegler, J.P. Biersack, and U. Littmark. *The stopping range of ions in solids, Vol. 1*. Pergamon Press, New York, 1985.

[110] B. G. Svensson, M. K. Linnarsson, B. Mohadjeri, M. Petravić, and J. S. Williams. SIMS and depth profiling of semiconductor structures. *Nuclear Instruments and Methods in Physics Research Section B: Beam Interactions with Materials and Atoms*, 85(1):363–369, 1994.

[111] C. Tian, Y. Xu, D. Nordlund, F. Lin, J. Liu, Z. Sun, Y. Liu, and M. Doeff. Charge heterogeneity and surface chemistry in polycrystalline cathode materials. *Joule*, 2(3):464–477, 2018.

[112] S.-L. Wu, W. Zhang, X. Song, A. K. Shukla, G. Liu, V. Battaglia, and V. Srinivasan. High Rate Capability of $Li(Ni_{1/3}Mn_{1/3}Co_{1/3})O_2$ Electrode for Li-Ion Batteries. *Journal of The Electrochemical Society*, 159(4):A438–A444, 2012.

[113] L. Wu, X. Xiao, Y. Wen, and J. Zhang. Three-dimensional finite element study on stress generation in synchrotron X-ray tomography reconstructed nickel-manganese-cobalt based half cell. *Journal of Power Sources*, 336:8–18, 2016.

[114] A. Devaraj, M. Gu, R. Colby, P. Yan, C. M. Wang, J. M. Zheng, J. Xiao, A. Genc, J. G. Zhang, I. Belharouak, D. Wang, K. Amine, and S. Thevuthasan. Visualizing nanoscale 3D compositional fluctuation of lithium in advanced lithium-ion battery cathodes. *Nature Communications*, 6:8014, 2015.

[115] L. Li, D. S. McPhail, N. Yakovlev, and H. Seng. Strategies for improving the sensitivity of FIB-SIMS. *Surface and Interface Analysis*, 43(1-2):495–497, 2011.

[116] D. S. McPhail, L. Li, Richard J. Chater, N. Yakovlev, and H. Seng. From FIB-SIMS to SIMS-FIB. The prospects for a 10 nm lateral resolution SIMS instrument with full FIB functionality. *Surface and Interface Analysis*, 43(1-2):479–483, 2011.

APPENDICES

Appendix A

The $Li_xNi_yCo_wMn_zO_2$ material used in this work is stoichiometric. However, its distribution is inhomogeneous at the atomic level. At the nanometre scale were the experiments in this study are made,we can assume the material is is statistically homogeneous in the regions of interest. Different stoichiometries than the one studied in this project would lead to a different chemistry of the material and therefore a change in emission of the individual elements due to matrix effect.

Appendix B

The Ga ion map distribution related to the analyses of figure 4.4 are added here for reference. Ga implantation is an unavoidable consequence of SIMS. Ga signal can be seen in the mass spectra presented in figure 4.1. The gallium peak observed is of small intensity compared to lithium signal. The primary Ga ion lose all their energy in the material, where ion implantation range in NMC at 30 keV can go up to 25 nm as calculated with TRIM software [[34]]. Therefore, the implanted Ga atoms can be sputtered in a subsequent frame of the analysis. This phenomenon is clearly seen in the depth distribution of figure 5.1. In the first 5 frames, gallium signal is null, since is being implanted only deeper in the material. This explains the presence of Ga signal in the mass spectra presented in the article.

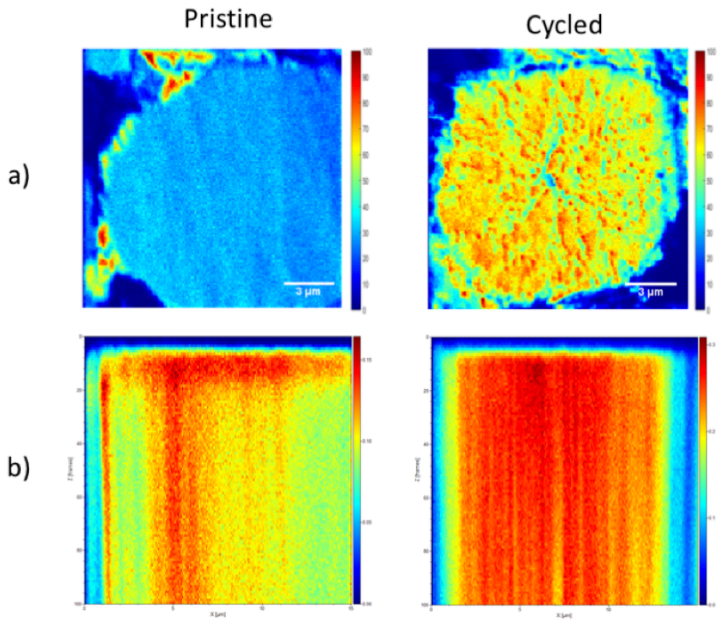

Figure 5.1 Galium ion distribution in pristine and cycled NMC. a) Normalized surface ion distribution over the 100 frames of the anlaysis and b) Ion depth distribution of Ga from 100 frames of analysis.